JNeurosci
THE JOURNAL OF NEUROSCIENCE

Research Articles | Development/Plasticity/Repair

Perisynaptic astroglial response to in vivo long-term potentiation and concurrent long-term depression in the hippocampal dentate gyrus.

https://doi.org/10.1523/JNEUROSCI.0943-25.2025

Received: 13 May 2025
Revised: 30 June 2025
Accepted: 1 August 2025

Title: Perisynaptic astroglial response to in vivo long-term potentiation and concurrent long-term depression in the hippocampal dentate gyrus.

Abbreviated title: Astroglial response to synaptic plasticity

Andrea J. Nam[1], Masaaki Kuwajima[1], Patrick H. Parker[1], Jared B. Bowden[1], Wickliffe C. Abraham[2], Kristen M. Harris[1]

[1]Department of Neuroscience, Center for Learning and Memory, University of Texas at Austin, Austin, TX 78712, United States

[2]Department of Psychology, University of Otago, Dunedin 9016, New Zealand

Corresponding author: Kristen M. Harris (email: kharris@utexas.edu)

Number of pages: 60

Number of figures: 12

Number of Tables: 0

Number of words for Abstract: 245

Number of words for Introduction: 650

Number of words for Discussion: 1494

Conflict of interest statement: The authors declare no conflicts of interest.

Acknowledgements:

We acknowledge that the tissue used in these studies were prepared as part of the thesis work reported in Bowden et al., 2012. We thank S.E. Mason-Parker for performing the in vivo electrophysiology and perfusions, J. Bowden for early work in the initiation of the experiments and early analyses, W. Yin for serial sectioning, tSEM imaging, and image alignment, J.M. Mendenhall for helping with tSEM imaging, B. Smith and L. Perry for initial serial sectioning and TEM imaging, L.F. Lindsey for helping with some of the original TrakEM2 image alignment, Dusten Hubbard for substantial tracing and editing of dendrites and spines, and J. Long for contributing to astroglia tracing. We also thank the team of students, including J. Ahn, S. Anand, P. Das, M. Ginjupalli, E. Haney, P. Mahableshwarkar, L. Robertson, and K. Rubenzer, who contributed to initial synapse and spine tracing efforts. The authors used ChatGPT (OpenAI) to assist with language editing and grammar correction during manuscript preparation. The authors acknowledge the Texas Advanced Computing Center (TACC, 3dem.org) at The University of Texas at Austin for providing computational resources that contributed to the results reported in this paper (URL: www.tacc.utexas.edu). Grant support: **NSF:** 2014862, 2219894; **NIH:** 1R56MH139176, 2R01MH095980

Abstract

Perisynaptic astroglia provide critical molecular and structural support to regulate synaptic transmission and plasticity in the nanodomain of the axon-spine interface. Three-dimensional reconstruction from serial section electron microscopy (3DEM) was used to investigate relationships between perisynaptic astroglia and dendritic spine synapses undergoing plasticity in the adult hippocampus. Delta-burst stimulation (DBS) of the medial perforant pathway induced long-term potentiation (LTP) in the middle molecular layer and concurrent long-term depression (cLTD) in the outer molecular layer of the dentate gyrus in awake male rats. The contralateral hippocampus received baseline stimulation as a within-animal control. Brains were obtained 30 minutes or 2 hours after DBS onset. An automated 3DEM pipeline was developed to enable unbiased quantification of astroglial coverage at the perimeter of the axon-spine interface. Under all conditions, >85% of synapses had perisynaptic astroglia processes within 120 nm of some portion of the perimeter. LTP broadened the distribution of spine sizes while reducing the presence and proximity of perisynaptic astroglia near the axon-spine interface of large spines. In contrast, cLTD transiently reduced the length of the axon-spine interface perimeter without substantially altering astroglial apposition. The postsynaptic density was discovered to be displaced from the center of the axon-spine interface, with this offset increasing during LTP and decreasing during cLTD. Astroglial access to the postsynaptic density was diminished during LTP and enhanced during cLTD, in parallel with changes in spine size. Thus, access of perisynaptic astroglia to synapses is dynamically modulated during LTP and cLTD alongside synaptic remodeling.

Significance Statement

Perisynaptic astroglia provide critical molecular and structural regulation of synaptic plasticity underlying learning and memory. The hippocampal dentate gyrus, a brain region crucial for learning and memory, was found to have perisynaptic astroglia at the axon-spine interface of >85% of excitatory synapses measured. Long-term potentiation triggered the retraction of perisynaptic astroglia processes selectively from large synapses. This retraction decreased access of perisynaptic astroglia to the postsynaptic density, which was discovered to be located off-center in the axon-spine interface. Concurrent long-term depression temporarily (< 2 h) decreased spine perimeter and thus increased access of synapses to perisynaptic astroglia. These findings provide new insights into how the structural dynamics of spines and synapses shape access to perisynaptic astroglia.

Introduction

Astroglia are complex cells that play essential roles in synaptic information processing (Semyanov and Verkhratsky, 2021). During development, they shape neuronal connectivity by participating in synapse formation and pruning (Risher et al., 2014; Chung et al., 2015; Allen and Eroglu, 2017; Lee et al., 2021; Tan et al., 2021; Saint-Martin and Goda, 2023). In the adult brain, astroglia support synaptic communication by maintaining ion homeostasis, removing excess glutamate, and supplying glutamine to neurons (Allen and Eroglu, 2017; Saint-Martin and Goda, 2023). Astroglial N-methyl-D-aspartate (NMDA) receptors regulate presynaptic strength (Letellier et al., 2016; Chipman et al., 2021), while calcium elevations (Shigetomi et al., 2013; Bindocci et al., 2017; Arizono et al., 2020) trigger the release of gliotransmitters, (including glutamate, ATP, and D-serine, that modulate synaptic activity) (Sahlender et al., 2014; Bazargani and Attwell, 2016; Fiacco and McCarthy, 2018; Lim et al., 2021; Letellier and Goda, 2023). These mechanisms are critical for synaptic function and position astroglia as key contributors in long-term potentiation (LTP) (Henneberger et al., 2010; Liu et al., 2022) and long-term depression (LTD) (Durkee et al., 2021)—cellular processes widely considered to underlie learning and memory.

Astroglial influence on synaptic activity is shaped by their structural relationship with pre- and postsynaptic components (Saint-Martin and Goda, 2023). Their highly branched morphology includes perisynaptic astroglial processes (PAPs), which comprise over 60% of the astroglial volume (Aboufares El Alaoui et al., 2021; Salmon et al., 2023). PAPs predominantly lie beyond the diffraction limit of conventional light microscopy (Rusakov, 2015) and display alternating constrictions and expansions (Salmon et al., 2023) that compartmentalize intracellular calcium transients (Bindocci et al., 2017; Arizono et al., 2020; Denizot et al., 2022).

Computational modeling indicates that PAP proximity impacts ionic homeostasis and rates of extracellular neurotransmitter diffusion (Kinney et al., 2013; Toman et al., 2023). Hence, a comprehensive analysis of astroglia-neuron structural relationships is essential for understanding the functional roles of astroglia during LTP and LTD.

The structural relationship between astroglia and neurons is dynamic over time and heterogeneous across brain regions. PAPs exhibit spontaneous motility and can undergo morphological changes in response to circuit-wide perturbations in neuronal activity (Hirrlinger et al., 2004; Bernardinelli et al., 2014; Perez-Alvarez et al., 2014). For example, in the hippocampal CA1 region, PAPs retract from excitatory synapses during LTP (Henneberger et al., 2020), whereas whisker stimulation increases astroglial coverage at synapses in the mouse somatosensory cortex (Genoud et al., 2006). Connectomic analyses suggest that astroglial coverage decreases at small, same-axon-same-dendrite synapse pairs with low size variance—features indicative of LTD (Yener et al., 2025). In parallel, single-cell RNA sequencing studies have identified 5-7 subtypes of protoplasmic astroglia across the hippocampus, striatum, and cortex (Batiuk et al., 2020; Endo et al., 2022). Marked morphological and molecular differences distinguish astroglia across cortical layers (Lanjakornsiripan et al., 2018). Thus, clarifying astroglial contributions to learning and memory also requires examining their structural relationships with neurons during synaptic plasticity in different brain areas.

In this study, we investigated astroglial apposition at the axon-spine interface (ASI) during LTP and LTD in the dentate gyrus—a hippocampal region critical for pattern separation and episodic memory, and one of the few areas where adult neurogenesis persists (Aimone et al., 2011; Hainmueller and Bartos, 2020; Denoth-Lippuner and Jessberger, 2021). Previous work using randomly selected photomicrographs demonstrated that astroglial coverage of synapses increases during LTP in the dentate gyrus molecular layer (Wenzel et al., 1991).

However, more recent studies have revealed that key features of astroglial nanostructure are lost with even moderate sectioning intervals in electron microscopy (Salmon et al., 2023). To overcome this limitation, we employed three-dimensional reconstruction from serial section electron microscopy (3DEM) coupled with a novel, automated method to measure PAP apposition at the ASI perimeter. Our results reveal that in the dentate gyrus, astroglial processes selectively withdraw from the ASI of large synapses during LTP, while maintaining close apposition to most synapses during LTD, regardless of synapse size.

Materials and Methods

Surgery

Data were collected from six adult male Long-Evans rats aged 121-185 days. In the experimental hemisphere of each animal, wire stimulating electrodes were surgically implanted into the medial and lateral perforant pathways of the angular bundle. In the contralateral control hemisphere, a single stimulating electrode was implanted into the medial perforant pathway only. Bilateral wire electrodes were also implanted into the dentate gyrus hilus to record field excitatory postsynaptic potentials (fEPSP). Full details of the surgical procedures can be found in Bowden et al. (2012).

Electrophysiology

Two weeks following surgery, 30-minute-long baseline recording sessions were commenced and carried out every two days until a stable baseline was achieved.

Baseline recording sessions (which were conducted during the animals' dark cycle and while the animals were in a quiet, alert state) consisted of constant-current biphasic square-wave test pulses (150 μs half-wave duration) delivered at a rate of 1 per 30 seconds. Test pulses were administered alternating between the three stimulating electrodes. Test pulse intensity was set to evoke medial path waveforms with fEPSP slopes ≥3.5 mV/ms in association with population spike amplitudes between 2 and 4 mV, at a stimulation current ≤500 μA. Once baseline recordings stabilized and following 30 minutes of test pulses, delta-burst stimulation (DBS) was delivered to the ipsilateral medial perforant path of the experimental hemisphere to induce LTP in the middle and cLTD in the outer molecular layer of the dentate gyrus (Bowden et al., 2012). The DBS protocol consisted of five trains of 10 pulses (250 μs half-wave duration) delivered at 400 Hz at a 1 Hz inter-train frequency, repeated 10 times at 1-minute intervals. The contralateral hemisphere received test pulses only to serve as within-subject control recordings. Following DBS, test pulse stimulation was resumed until the animal was sacrificed at either 30 min or 2 h following DBS onset depending on the experimental group (3 animals per group). The initial slopes of the medial and lateral path fEPSPs were measured for each waveform and expressed as a percentage of the average response during the last 15 min of recording before DBS (Fig. 1A-C).

Perfusion and Fixation

Animals were perfusion-fixed under halothane anesthesia and a tracheal supply of oxygen (Kuwajima et al., 2013a). The perfusion protocol consisted of a brief (~20 s) wash with oxygenated Krebs-Ringer Carbicarb buffer (concentration (in mM): 2.0 $CaCl_2$, 11.0 D-glucose, 4.7 KCl, 4.0 $MgSO_4$, 118 NaCl, 12.5 Na_2CO_3, 12.5 $NaHCO_3$; pH 7.4; Osmolality: 300-330 mmol/kg), followed by 2% formaldehyde and 2.5% glutaraldehyde in 0.1 M cacodylate buffer (pH 7.4) containing 2 mM $CaCl_2$ and 4 mM $MgSO_4$ for approximately 1 hour (~2 L of fixative per animal). Brains were removed from the skull around 1-hour post-perfusion, wrapped in layers of cotton gauze, and then shipped by overnight delivery (TNT Holdings B.V.) in the same fixative from the Abraham Laboratory in Dunedin, New Zealand to the Harris Laboratory in Austin, Texas.

Tissue Processing and Serial Sectioning

The fixed tissue was sliced using a vibrating blade microtome (Leica Microsystems) along the parasagittal plane into 70 µm thick slices (Fig. 1D). The slice containing the recording electrode and its two neighboring slices were processed for electron microscopy as described previously (Harris et al., 2006; Kuwajima et al., 2013a; Bromer et al., 2018). In summary, the tissue was treated with reduced osmium (1% osmium tetroxide and 1.5% potassium ferrocyanide in 0.1 M cacodylate buffer with 2 mM Ca^{2+} and 4 mM Mg^{2+}) followed by microwave-assisted incubation in 1% osmium tetroxide under vacuum. Next the tissue was subjected to microwave-assisted dehydration and en bloc staining with 1% uranyl acetate in ascending concentrations of ethanol. The dehydrated tissue was embedded into LX-112 epoxy resin (Ladd Research) at 60°C for 48 h. Then the tissue-containing resin blocks were cut into ultra-thin sections at the nominal thickness of 45 nm with a 35° diamond knife (DiATOME) on an ultramicrotome

(Leica Microsystems). For 4 of the 6 animals, the MML and OML regions were sectioned ~125 µm and ~250 µm from the top of the granule cell layer in the dorsal blade of the hippocampal dentate gyrus (Fig. 1D, d_i). For the remaining 2 animals, the tissue was sectioned at a 26.6° angle relative to the granule cell layer, allowing many MML and OML dendrites to be cut in cross-section. This new sectioning approach was developed to capture both layers within the same set of ultra-thin serial sections (Fig. 1D, d_{ii}). This new approach was more efficient but did not introduce any sampling biases as both dentate molecular layers were sampled. The ultra-thin tissue sections were collected onto Synaptek Be-Cu slot grids (Electron Microscopy Sciences or Ted Pella), coated with Pioloform (Ted Pella), and finally stained with a saturated aqueous solution of uranyl acetate followed by lead citrate (Reynolds, 1963).

Imaging

The ultra-thin serial tissue sections were imaged, blinded as to experimental condition (Fig. 1D). Tissue from 4 of the 6 animals was imaged with a JEOL JEM-1230 TEM to produce 16 EM image series (2 series per condition). Tissue from the remaining 2 animals was imaged with a transmission-mode scanning EM (tSEM) (Zeiss SUPRA 40 field-emission SEM with a retractable multimode transmitted electron detector and ATLAS package for large-field image acquisition), to produce 8 EM image series (1 series per condition) (Kuwajima et al., 2013a, 2013b). Sections imaged with TEM were captured in two field mosaics at 5,000x magnification with a Gatan UltraScan 4000 CCD camera (4,080 pixels × 4,080 pixels) controlled by Digital Micrograph software (Gatan).

These mosaics were then stitched together post-hoc using the Adobe Photoshop Photomerge function. On the tSEM, each section was imaged with the transmitted electron detector from a single field encompassing up to 32.768 µm × 32.768 µm (16,384 pixels × 16,384 pixels at 2 nm/pixel resolution). The scan beam dwell time was set to 1.3-1.4 ms and the accelerating voltage was set to 28 kV in high-current mode.

Alignment

Serial TEM images were first manually aligned in legacy Reconstruct (Fiala, 2005). Then the initial round of automatic alignment for all image volumes was completed using the TrakEM2 Fiji plugin (Cardona et al., 2012; Saalfeld et al., 2012; Schindelin et al., 2012). Images underwent rigid alignment, followed by affine alignment, and then elastic alignment. These new alignments were applied permanently to the images. Next the TrakEM2 aligned image volumes were automatically aligned again using AlignEM SWiFT, a software that aligns serial section images using Signal Whitening Fourier Transform Image Registration (SWiFT-IR) (Wetzel et al., 2016). Finally, image volumes were subjected to further regional, by-dendrite alignments to overcome local artifacts (stretches, tears, or folds) using Reconstruct's modern replacement PyReconstruct, an open-source Python-based software for serial EM analysis (https://github.com/SynapseWeb/PyReconstruct). All image series in the dataset were given a five-letter code to blind investigators as to the experimental condition. The grating replica (0.463 µm per square; Ernest Fullam, Inc., Latham, New York) image was acquired along with serial sections and used to calibrate pixel size for each series.

In addition, the section thickness was estimated using the cylindrical diameters method and found to be 42-55 nm, close to the nominal setting (45 nm) on the ultramicrotome (Fiala and Harris, 2001a).

Unbiased Annotation of Tripartite Synapses

Previous work has demonstrated that the average number of dendrite microtubules scales linearly with dendrite diameter and the number of spines per micron length of dendrite (Fiala and Harris, 2001b; Harris et al., 2022). Therefore, in each image volume from every layer of the dentate gyrus in each animal, three dendrites of comparable caliber were chosen based on the average microtubule count for that layer (average microtubule count per dendrite: OML – 20-25; MML – 30-35). A total of 72 dendrites and 2,083 excitatory synapses were analyzed for the 24 series in this dataset.

Object annotations were completed while masked to condition using legacy Reconstruct (Fiala, 2005) and PyReconstruct. Annotation files (.ser) created using legacy Reconstruct were updated to the PyReconstruct file format (.jser). Dendritic spine contours were manually traced from each selected dendrite. Postsynaptic densities (PSD) of excitatory synapses were identified based on their asymmetric, high-contrast electron densities and the presence of clear, round presynaptic vesicles in the presynaptic axonal bouton (Harris and Weinberg, 2012). The PSD area was measured in PyReconstruct according to the specific sectioning orientation, as previously described in Harris et al. (Harris et al., 2015). PAPs, characterized by their tortuous morphology, relatively clear cytoplasm (Fig. 2A), and glycogen granules on serial sections (Witcher et al., 2007), were traced if they fell within 1 μm of a synaptic profile center. Given that synapses can interact with all astroglial compartments (Aten et al., 2022), the annotated PAPs consisted of both thick astroglia branches and terminal leaflets (Semyanov and Verkhratsky, 2021; Salmon et al., 2023). Along the z-axis, both PAPs and presynaptic axons were traced throughout the range of sections where the ASI was visible, plus an additional 1-2 sections beyond the ASI in both directions. In the x-y plane, axons were traced until the bouton tapered into a vesicle-free region.

Rare dually innervated spines (with both excitatory and inhibitory synapses) were excluded from analyses (Villa et al., 2016; Kleinjan et al., 2023). Likewise, synapses were omitted if local section flaws or proximity to image volume boundaries prevented accurate and complete PAP segmentations.

3D Reconstruction: Mesh Generation and Processing

3D watertight mesh analysis was completed using Blender, a free, open-source computer graphics tool with a Python interface. Spine and axon objects were reconstructed from serial section traces using Neuropil Tools (https://github.com/mcellteam/neuropil_tools), a Blender add-on, in the MCell/CellBlender v4.0.6 bundle for Blender 2.93. Any incorrectly meshed objects were manually fixed using native Blender mesh editing tools before being exported in the Polygon File Format (PLY) for 3D objects. Exported meshes were re-meshed using the isotropic re-meshing function within the Computational Geometry Algorithms Library (CGAL) 5.0.2 Polygon Mesh Processing package (https://www.cgal.org). This tool converts faulty meshes into manifold and watertight meshes with outward-facing normal vectors. For the re-meshing routine, the number of iterations was set to 3 and the target edge length parameter was set to 0.04. All object meshes were then smoothed using GAMer2, a 3D mesh processing software that conditions surface meshes to correct for artifacts such as jagged boundaries and high aspect ratio faces (Lee et al., 2020). All axon meshes met a face density threshold of at least 10,000 faces per volume (Fig. 2B). The spine volumes were estimated in Blender using the Blender add-on, 3D Print Toolbox (https://extensions.blender.org/add-ons/print3d-toolbox).

PAPs and synapses were reconstructed using PyReconstruct, which uses trimesh to generate triangulated meshes with watertight surfaces (https://trimesh.org). Synapses were reconstructed from contact traces, drawn around each PSD area trace, and extended just beyond the spine membrane contour to enable visualization (Fig. 2A). All astroglial and synapse meshes were imported into Blender in the correct by-dendrite alignment as PLY files.

Linear tissue shrinkage can occur with chemical fixation for electron microscopy, which is thought to be accounted for by the loss of extracellular space (Kalimo, 1976; Kirov et al., 1999; Kinney et al., 2013; Korogod et al., 2015; Tønnesen et al., 2018). Since it is not possible to quantify the effects of fixation and all tissue samples underwent the same fixation and processing protocols, the 3D reconstructions were evaluated without arbitrary correction for potential swelling or shrinkage.

Automated 3D Analysis of Astroglial Apposition at the ASI Perimeter

An automated analysis pipeline was developed to measure astroglial apposition at the ASI perimeter. The algorithm was developed in Blender 3.6.5, using Blender's Python API.

Stage 1: ASI Identification

Since the axon mesh was more uniformly shaped than the spine mesh, the ASI was identified from the axon mesh faces based on two criteria (Fig. 2C, D). First, the projected normal vector from a given axon face (f_{ai}) had to intersect a face (f_{si}) on the apposing spine mesh. Second, the Euclidean distance between the f_{ai} center and apposing f_{si} center had to be less than a pre-determined maximum distance threshold (d_{ASI}). For this study, $d_{ASI} \leq 45$ nm was used (Fig. 2C).

Stage 2: Measurement of the ASI area and Perimeter

The set of edges surrounding the triangulated ASI faces was extracted (Fig. 2E, F). Then the Relax function from the Loop Tools Blender add-on (https://extensions.blender.org/add-ons/looptools/) was used to smooth the boundary loop of edges over 10 iterations. The ASI perimeter was calculated by summing the lengths of each edge comprising the final ASI boundary (Fig. 2D-F). Similarly, the ASI area was determined by summing the areas of each face enclosed by the final ASI boundary.

Stage 3: Measurement of Astroglial apposition at the ASI perimeter

The Euclidean distance from each ASI boundary edge midpoint to the nearest point on the PAP mesh (d_{ag}) was measured. Then the lengths of all ASI edges with d_{ag} less than or equal to a pre-determined distance threshold were summed to give the length of the ASI perimeter surrounded by astroglia (l_{ag}) (Fig. 2G). Astroglial proximity to the ASI perimeter was quantified by averaging d_{ag} across all ASI perimeter edges with $d_{ag} \leq 120$ nm. The upper limit of $d_{ag} \leq 120$ nm was chosen to ensure that the PAPs had an unobstructed extracellular diffusion path to the ASI perimeter (Fig. 2H, I).

For this study, l_{ag} measurements were made based on distance thresholds ranging from $d_{ag} \leq 10$ to 120 nm, in 10 nm increments (Fig. 2G, J), balancing spatial resolution limitations and functional relevance. With an x-y resolution of ~2 nm per pixel and an axial resolution of ~45 nm, a lower limit of $d_{ag} \leq 10$ nm minimized anisotropy-related errors.

Categorizing the Location of Astroglial Apposition

Synapses with astroglia within the 120 nm (upper limit discussed above) of the ASI perimeter were assigned to the ASI^{ag+} category. All remaining synapses (ASI^{ag-}) were categorized based on astroglial apposition present at both pre- and postsynaptic elements but not at the ASI (Pre-Post), only at the presynaptic bouton (Pre), only at the postsynaptic spine (Post), or absent from all these locations (None). This subsequent classification was determined by examining the serial EM images to identify astroglial contact with the postsynaptic spine, the presynaptic bouton, or both.

Measurement of PSD Offset

For each synapse, the ASI faces were duplicated, separated from the axon object, and converted into a new ASI surface mesh. Each PSD object was also duplicated and conformed to the axon surface using Blender's native shrink-wrap mesh modifier (ax-PSD object). Then the geometric centroids of the ASI surface and ax-PSD meshes were calculated by averaging the coordinates of their respective vertices. PSD offset was defined as the Euclidean distance between these centroids.

For ASI^{ag+} synapses only, the average distance from astroglial apposition at the ASI to the nearest PSD edge ($d_{agASI\text{-}PSD}$) was estimated by averaging the Euclidean distances from each ASI perimeter edge midpoint with $d_{ag} \leq 120$ nm to the nearest point on the ax-PSD object. Meanwhile, the overall ASI perimeter-to-PSD distance ($d_{ASI\text{-}PSD}$) was calculated by averaging the Euclidean distances from all ASI perimeter edge midpoints to the nearest point on the ax-PSD object. Synapses were classified as ag-proximal ($d_{agASI\text{-}PSD} < d_{ASI\text{-}PSD}$) or ag-distal ($d_{agASI\text{-}PSD} \geq d_{ASI\text{-}PSD}$). Additionally, the ratio of $d_{agASI\text{-}PSD}$ to $d_{ASI\text{-}PSD}$ served as an alternative measure of PSD offset, incorporating directional information relative to astroglial apposition at the ASI.

Unit Conversion

For each EM image series, a reference circle with a known, calibrated radius of 1 µm was stamped in PyReconstruct and imported into Blender as a two-dimensional object. The reference circle's radius was measured in Blender (r_b), and all subsequent Blender measurements were multiplied by a factor of 1 µm/r_b to ensure accurate scaling to microns.

Experimental Design

As described above for Fig. 1, 3 animals were prepared for serial EM analysis at each of the two time points after the induction of LTP and cLTD. For each time point and condition, 3 dendrites of comparable caliber were selected for 3D reconstruction and analysis. To avoid introducing variance related to the correlation between spine density and dendrite caliber, we used the unbiased dendritic length (length of the dendritic segment extending from the first spine origin to the beginning of the last spine origin) to sample dendrites instead of randomly sampling the neuropil (Fiala and Harris, 2001b). To assess differences between LTP and control or cLTD and control, a mixed model was used with random effects for animal and dendrite included to account for inter-animal and inter-dendrite variability.

Statistical Analyses

All statistical analyses and graphical plots were completed in RStudio using R version 4.4.1. All kernel density estimate (KDE) plots showing the probability density function (PDF) for parameters of interest were generated using geom_density()(ggplot2 package in R) with the default bandwidth calculated by stats::density()(adjust = 1). The PDF represents the distribution of the variable such that the area under the curve sums to 1. Thus, the y-axis of the corresponding KDE plot reflects density values that vary with the shape and spread of the data, and do not necessarily range from 0 to 1.

Data clustering was conducted based on ASI perimeter and spine volume with conditions and time points pooled, but separately for MML and OML data. The silhouette method determines the optimal number of clusters (k) by measuring object similarity to its cluster compared to other clusters, with values ranging from -1 to 1 indicating bad to good data clustering. Iterating over k = 2 to 20, we determined that the optimal number of clusters was k = 2 for both layers using the silhouette function from the cluster package (version 2.1.6) in R. Then, we performed k-means clustering to separate the data into two clusters: cluster 1 (c1) and cluster 2 (c2). For the clustering algorithm, the maximum number of iterations allowed was set to 10 and the number of random sets to be chosen was set to 25.

Relative synapse percentages in each astroglia-ASI apposition category (ASI^{ag+}/ASI^{ag-}) or cluster category (c1/c2) were compared using Pearson's Chi-squared (χ^2) test with Yates' continuity correction applied. Variable sample distributions were compared using a Kolmogorov-Smirnov (KS) test with a two-sided alternative hypothesis. Comparisons of means and linear regressions were conducted using the lmerTest package for R (Kuznetsova et al., 2017).

Linear mixed models (LMM) were fitted to the data with additive random intercepts for animal and dendrite included to account for variability at these group levels. To meet

LMM assumptions of normality and homoscedasticity, the following data transformations were applied during analysis: log-transformations (applied to spine volume, average d_{ag}, PSD area, ASI area, PSD offset, PSD-to-ASI area ratio, average $d_{agASI\text{-}PSD}$, and average $d_{ASI\text{-}PSD}$ data) and square-root transformations (applied to ASI perimeter and l_{ag} data). Transformations of ASI perimeter data were applied only when ASI perimeter served as the response variable, not as a covariate predictor in the model. To limit data-based multicollinearity, numerical covariates were mean-centered. For comparisons across astroglia-ASI apposition categories, condition, clusters, PSD offset direction, and layer, the reference categories were defined as ASI^{ag-}, control, cluster 1, ag-distal, and MML synapses, respectively. Model goodness-of-fit was assessed using the marginal coefficient of determination (R^2), which represents the ratio of explained variance (Sum of Squares Regression, SSR) over total variance (Sum of Squares Total, SSTO). R^2 was calculated using the r.squaredGLMM function from the MuMIn package in R. Effect sizes of individual predictors were quantified using partial eta² (η_p^2). All p-values from multiple comparisons were adjusted using the Benjamini-Hochberg (BH) procedure to control the False Discovery Rate (FDR).

The significance level was set at $\alpha = 0.05$. Potential outliers were identified as values falling more than 1.5 times the interquartile range below the first quartile or above the third quartile. However, outliers were only excluded from analyses if manual inspection confirmed they were due to measurement errors.

Code Accessibility

All code for the automated ASI detection and assessment of astroglial apposition is hosted on GitHub (code available at: https://github.com/ajnam03/asi_blender.git).

Results

Apposition of perisynaptic astroglial processes (PAPs) at MML synapses

MML synapses were reconstructed from serial EM images (Fig. 3A, B), and an automated 3D analysis method was developed to evaluate astroglial coverage within 10 to 120 nm of the ASI perimeter (Methods). Synapses were categorized based on the presence (ASI^{ag+}) or absence (ASI^{ag-}) of astroglia within 120 nm of the ASI perimeter. Then ASI^{ag-} synapses were further subdivided by the astroglial location beyond the ASI perimeter (Fig. 3C). The percentage of ASI^{ag+} synapses varied depending on the specific distance threshold used (Fig. 3D, insets). However, approximately 60% of MML synapses had astroglial apposition within 10 nm of the ASI, 70-80% had astroglial apposition within 30 nm, and more than 90% had astroglial apposition within 120 nm at both time-points in both control and LTP hemispheres (Fig. 3D). Thus, synapses with astroglial apposition within 10, 30, or 120 nm were assessed in all subsequent analyses. No synapses were entirely devoid of astroglial contact at all locations. These findings indicate that most MML synapses were tripartite at some portion of their ASI perimeter under control and LTP conditions.

Enlargement of spines and expansion of ASI during LTP

At 30 minutes and 2 hours during LTP, a shift toward larger spine volumes was observed, regardless of whether astroglia occurred within 10, 30, or 120 nm of some portion of the ASI (Fig. 3E). Similarly, the distribution of the ASI perimeter—the specific length of the interface accessible to PAP—shifted rightward at 2 hours (Fig. 3F). Both the mean spine volume and ASI perimeter were also significantly elevated at 2 hours compared to control (Fig. S1A, B; Table S2). Interestingly, synapses with astroglial apposition had larger spine volumes and ASI perimeters than those without astroglial contact at 30 minutes in control and at both time points during LTP (Fig. S1A, B). Together, these results suggest that both spine volume and ASI perimeter—two measures of spine size—increased during LTP at MML tripartite synapses.

K-means clustering based on spine volume and ASI perimeter in MML

It is notable that the spine volume and ASI perimeter distributions showed distinct bimodal shapes during LTP, suggesting that LTP could preferentially affect sub-populations of spines (Fig. 3E, F). Using the silhouette method and k-means clustering, two clusters of MML ASI^{ag+} synapses were identified based on spine volume and ASI perimeter (Fig. 3G). Cluster 2, which accounted for 27% of MML ASI^{ag+} synapses, had larger spine volumes and ASI perimeters than cluster 1 synapses (Table S1). The proportion of cluster 2 synapses significantly increased at 30 minutes and 2 hours during LTP. Spine volume and ASI perimeter were positively correlated across synapse clusters under both experimental conditions (Fig. 3G). Hence, in all subsequent work, regression analyses were done independently for these distinct clusters of small and large spines.

Sustained spine enlargement displaces PSD from ASI center during LTP

The PSD—an electron-dense region enriched with proteins critical for synaptic transmission and plasticity—was displaced from the ASI center by 47-57 nm under control conditions (Fig. 4A, B). During LTP, the distribution of PSD areas broadened and remained elevated for at least 2 hours (Figs. 4C, S1C), and the PSD's offset increased significantly at 2 hours (Figs. 4D, S1D). Both PSD area and offset were positively correlated with ASI area, and after controlling for spine size, no direct effect of LTP on either measure was detected (Fig. 4E, F). In contrast, PSD area and offset showed only weak and inconsistent relationships with the extent of astroglial coverage (Fig. S2A, C), astroglial distance from the ASI perimeter (Fig. S2B, D), and with each other (Fig. S2E). These findings suggest that LTP increased the prevalence of both small and large synapses, and that the associated spine enlargement contributed to greater PSD offset from the ASI center.

Decrease in astroglial surround at ASI perimeter of large synapses during LTP

To assess the impact of LTP on astroglial apposition, the length of the ASI perimeter surrounded by astroglia was measured as depicted in Figures 2G and 5A. On average, astroglia surrounded only 50% of the ASI perimeter and did not fully envelop any MML synapses (Fig.

S3A). The mean length of astroglial surround was positively correlated with total ASI perimeter for both small and large spine clusters (Fig. 5B, C). By 30 minutes and 2 hours after LTP induction, the extent of astroglia surrounding the ASI perimeter was reduced for cluster 2 synapses across all distance thresholds from 10-120 nm, but not for cluster 1 synapses (Fig. 5B, C). Therefore, these results indicate that as spines and their ASI perimeters enlarged during LTP, a smaller proportion of their interface remained in contact with surrounding astroglial processes.

Increase in minimum astroglial distance to the ASI perimeter at large synapses during LTP

To evaluate changes in astroglial proximity during LTP, the minimum distance from the ASI perimeter to the nearest astroglial process was measured for all vertices with $d_{ag} \leq 120$ nm (see Figs. 2J, 5D; Methods). Astroglia processes were 46-48 nm from the ASI perimeter, and this minimum distance did not differ between control and LTP when all MML synapses were analyzed together (Fig. S3B). For cluster 2 synapses, however, the mean minimum astroglial distance remained unchanged at 30 minutes (Fig. 5E) but was significantly increased at 2 hours during LTP across all distance thresholds (10-120 nm) (Fig. 5F). This suggests that in addition to reducing their length of surround, astroglial processes gradually withdrew from the ASI perimeter of large synapses during LTP.

Decrease in PSD access to PAPs due to ASI enlargement during LTP

PAPs rarely, if ever, have direct physical access to the PSD itself because the ASI surrounds the PSD. Therefore, to examine whether LTP affects PSD access to perisynaptic astroglia, we measured the average distance from the PSD to the region of the ASI perimeter contacted by PAPs within 120 nm ($d_{agASI-PSD}$; Fig. 5G; Methods). This PSD-to-astroglia distance significantly increased by 2 hours during LTP (Fig. 5H) and was positively correlated with both the PSD-to-overall ASI perimeter distance ($d_{ASI-PSD}$, Fig. 5I) and ASI area (Fig. 5J). Notably, the PSD-to-astroglia distance scaled nearly one-to-one with the PSD-to-ASI perimeter distance under both control and LTP conditions, suggesting no preferential displacement toward or away from astroglial apposition (Fig. 5I). After controlling for ASI area, the effect of LTP on the PSD's distance to astroglial apposition was no longer observed (Fig. 5J). Approximately 33-35% of all MML ASI^{ag+} synapses had $d_{agASI-PSD} < d_{ASI-PSD}$ (ag-proximal, Fig. S3C), but no significant differences were found between control ag-proximal and ag-distal ($d_{agASI-PSD} \geq d_{ASI-PSD}$) synapses in mean spine volume (Fig. S3D), ASI perimeter (Fig. S3E), or PSD area (Figs. S3F). Together, these results indicate that, in addition to increasing PSD offset, spine enlargement during LTP also reduced astroglial access to the PSD.

PAP apposition at OML synapses

By applying the same strategies in the OML as used to analyze MML synapses (Fig. 6A-C; Methods), we found that more than 85% of synapses had astroglia within 120 nm of some region of the ASI perimeter, with around 60% having astroglia within 10 nm (Fig. 6D). Hence, like in the MML, the majority of OML synapses showed close astroglial apposition under control and cLTD conditions, and synapses with astroglial apposition within 10, 30, or 120 nm were included in all subsequent analyses.

Transient increase in relative frequency of synapses with shorter ASI perimeters during cLTD

Both spine volume and the length of the ASI perimeter were greater at synapses with astroglia present along some portions of the ASI perimeter under control and cLTD conditions (Fig. S4A, B). Although cLTD did not significantly affect spine volume (Figs. 6E, S4A), the distribution of ASI perimeter lengths shifted leftward at 30 minutes—but not at 2 hours—reaching statistical significance when astroglia located within 120 nm were included (Fig. 6F). These results suggest that while spine volume remained stable during cLTD, there was a transient increase in the relative prevalence of synapses with shorter ASI perimeters.

K-means clustering based on spine volume and ASI perimeter in the OML

Similar to the MML, OML ASI^{ag+} synapses were grouped into two clusters based on spine volume and ASI perimeter (see Methods). Cluster 2 synapses, comprising 15% of OML ASI^{ag+} synapses, had larger spine volumes and ASI perimeters compared to cluster 1 synapses (Fig. 6G). The relative proportion of cluster 2 synapses remained stable between control and cLTD conditions (Table S1). Spine volume and ASI perimeter were also positively correlated across synapse clusters, with no observed effect of cLTD on this relationship (Fig. 6G). Therefore, once again, in all subsequent regression analyses of OML synapses, these unique clusters of small and large spines were analyzed separately.

Transient ASI perimeter shrinkage temporarily decreases PSD offset from the ASI center during cLTD

Although cLTD had minimal effect on PSD area (Figs. 7A-C, S4C), PSD offset from the ASI center—47-54 nm under control conditions—was significantly reduced at 30 minutes during cLTD (Figs. 7D, S4D). As in the MML, both PSD area and offset were positively correlated with ASI area (Fig. 7E, F). Moreover, after controlling for spine size, the effect of cLTD on PSD displacement was no longer evident (Fig. 7F). Neither PSD area nor PSD offset showed consistent relationships with the length of astroglial surround (Fig. S5A, C), the astroglial distance to the ASI perimeter (Fig. S5B, D), or with each other (Fig. S5E). Taken together, these findings suggest that during cLTD, the transient decrease in ASI perimeter coincided with a higher prevalence of synapses with more centrally located PSDs within the ASI, independent of the extent of astroglial apposition.

Stable amount of PAP surrounding the ASI perimeter during cLTD

Evaluation of OML ASI^{ag+} synapses revealed that most had about 50% of the length of their ASI perimeters surrounded by astroglial processes (Figs. 8A, S6A). Additionally, the length of the apposition correlated positively with ASI perimeter across synapse clusters (Fig. 8B, C). At 2 hours during cLTD, significant interactions between condition and ASI perimeter influenced the mean length of astroglial surround for cluster 2 synapses across all distance thresholds from 10-120 nm (Fig. 8C). However, no cLTD-related effects were found at 30 minutes, nor for cluster 1 synapses at either time point. These results indicate that the extent of astroglial apposition at the ASI perimeter remained largely unchanged during cLTD.

Transient decrease in minimum PAP distance to the ASI perimeter during cLTD

On average, astroglial processes apposed OML synapses at a minimum distance of 49 nm (Fig. 8D). No significant differences in the mean PAP apposition distance were observed between control and cLTD conditions when OML synapses were analyzed collectively (Fig. S6B), and this minimal distance did not correlate with ASI perimeter across synapse clusters (Fig. 8E, F). Nonetheless, for cluster 1 synapses with astroglia within 30 nm of the ASI, the mean minimum PAP distance to the ASI was significantly decreased at 30 minutes during cLTD (Fig. 8E). Significant interactions between condition and ASI perimeter were also observed for cluster 1 synapses with astroglia within 10 nm at both 30 minutes and 2 hours, and within 30 nm at 30 minutes (Fig. 8E, F). Therefore, the transient spine morphology changes associated with cLTD were accompanied by modest but specific increases in astroglial proximity, particularly at distances close to the ASI.

Transient increase in astroglial access to the PSD during cLTD

At 30 minutes during cLTD, the average distance from the PSD to the region of the ASI perimeter apposed by astroglia was transiently reduced (Fig. 8G, H). As observed in the MML, this distance correlated positively with the PSD's offset from the overall ASI perimeter, with a slope close to one under both control and cLTD conditions–indicating that astroglial positioning does not bias the direction of PSD displacement (Fig. 8I). After controlling for ASI area, the effect of cLTD on the PSD-to-astroglia distance was no longer significant (Fig. 8J). Approximately 34-35% of OML ASI^{ag+} synapses had their PSD positioned closer to the astroglia-apposed region of the ASI perimeter ($d_{agASI\text{-}PSD} < d_{ASI\text{-}PSD}$; Fig. S6C). However, no significant differences in mean spine volume (Fig. S6D), ASI perimeter (Fig. S6E), or PSD area (Fig. S6F) were observed between ag-proximal versus ag-distal ($d_{agASI\text{-}PSD} \geq d_{ASI\text{-}PSD}$) OML synapses under either control or cLTD conditions. Overall, these findings suggest that spine morphology changes associated with cLTD temporarily enhanced astroglial access to the PSD.

Comparable amount of perisynaptic astroglia at MML and OML control synapses

To test whether inherent baseline differences between control MML and OML layers were responsible for the observed differences between effects of LTP and cLTD at dentate gyrus synapses, we repeated all the analyses by comparing MML and OML ASI^{ag+} synapses under control conditions, with the 30 minute and 2 hour time points pooled.

The proportion of synapses with astroglial apposition at the ASI did not differ between the dentate gyrus layers (Fig. 9A). However, the MML had a higher relative percentage of cluster 2 synapses compared to the OML (Fig. 9B). ASI perimeters were comparable between layers (Fig. 9C), whereas PSD areas were larger in the MML than in the OML (Fig. 9D). An interaction between layer and ASI perimeter influenced the mean minimum PAP distance to the ASI for cluster 1 synapses (Fig. 9E). In contrast, this distance for cluster 2 synapses (Fig. 9E), as well as the average fraction of astroglial surround for either cluster (Fig. 9F), did not significantly differ between layers. No significant differences were observed for the distributions of PSD offset (Fig. 9G) and astroglial distance to the PSD (Fig. 9H).

Finally, the ASI perimeter (Fig. 10A) and PSD area (Fig. 10B) distributions differed significantly during LTP versus cLTD. However, condition and layer did not interact to influence either the mean length of astroglial surround (Fig. 10C) or PAP distance to the ASI perimeter (Fig. 10D). LTP and cLTD conditions also showed significant differences in PSD offset (Fig. 10E) and average PAP distance to the PSD (Fig. 10F). Together, these results suggest that, while some baseline differences exist between molecular layers, they are unlikely to explain the different LTP- and cLTD-related changes observed in this study.

Discussion

We found that most dendritic spines in the dentate gyrus have perisynaptic astroglia at their ASI perimeter. While the proportion of tripartite synapses remained stable during LTP or cLTD, PAP proximity to synapses was modulated by synaptic plasticity (Figs. 11, 12). LTP expanded the range of spine volumes, resulting in a net increase in large spines and PSD areas, the latter noted for the first time as an offset from the ASI center (Fig. 11A). Reduced astroglial proximity to the ASI perimeter of enlarged synapses decreased astroglial access to the PSD (Fig. 12A). Meanwhile, cLTD produced subtle reductions in spine volume, PSD area, and PAP proximity to the ASI (Figs. 11B, 12B). During cLTD, there was a transient decrease in

ASI perimeter length, possibly reflecting reduced spine complexity that would enhance astroglial-PSD access (Fig. 12B).

We developed a novel 3D approach to establish reliable criteria to investigate astroglial-synapse relationships on dendritic spines. Application of this or similar approaches will be needed to compare astroglial coverage across brain regions. For example, in the dentate gyrus, we showed that the percentage of tripartite synapses varied substantially depending on the apposition criteria used, ranging from 60% of synapses with astroglia within 10 nm of the ASI perimeter to 85% within 120 nm. This latter value surpasses prior estimates from single-section analyses, which reported < 40% of dentate gyrus synapses with astroglia at their ASI perimeters (Wenzel et al., 1991). Single-section sampling fails to capture that most synapses are surrounded by astroglia, inadvertently misclassifying those with partial apposition as lacking PAP coverage.

To define a functionally relevant threshold for astroglial apposition, we restricted our analyses to synapses with astroglia ≤120 nm from the ASI perimeter. Mathematical models indicate that astroglial apposition within 150 nm increases glutamate uptake, diminishing AMPA receptor currents by 50% (Pannasch et al., 2014). Chemical fixation can cause shrinkage of extracellular space (Korogod et al., 2015). The 150 nm threshold did not account for this shrinkage, nor did it account for the intervening neuropil structures that limit PAP apposition. Accordingly, our 120 nm threshold reflects a conservative functional estimate of astroglial access to synapses.Our findings in the dentate gyrus contrast with previous 3DEM studies in hippocampal area CA1, where PAP apposed approximately 62% of synapses (Ventura and Harris, 1999; Witcher et al., 2007). Reports of astroglial coverage exceeding 80% of CA1 synapses may reflect less stringent criteria for apposition, potentially including PAPs separated from the ASI by surrounding structures (Chai et al., 2017; Gavrilov et al., 2018). Additionally, the fraction of neuropil occupied by astroglia is often higher near smaller synapses (Medvedev et al., 2014; Gavrilov et al., 2018). Thus, differences in spine and synapse size may underlie the disparity in astroglial coverage between the smaller synapses in the dentate gyrus and those spanning a broader size range in area CA1 (Harris and Stevens, 1989).

In the dentate gyrus, both LTP and cLTD led to significant morphological changes at tripartite synapses. LTP expanded the range of spine and PSD sizes, consistent with prior findings (Bromer et al., 2018). Meanwhile, cLTD in the OML did not produce the spine shrinkage previously observed with LTD in CA1 (Okamoto et al., 2004; Zhou et al., 2004). Instead, we observed more spines with shorter ASI perimeters but not necessarily smaller volumes, suggesting a temporary shift toward less complex spine morphologies during cLTD.

Our findings suggest that astroglia maintain a delicate balance between insufficient and excessive synapse coverage to establish a permissive environment for synaptic plasticity. LTP and cLTD-associated changes occurred primarily at synapses with astroglial apposition. Furthermore, consistent with previous findings (Witcher et al., 2007; Bellesi et al., 2015), mean spine and synapse size were larger for synapses associated with PAP. In contrast, no dentate gyrus synapse exhibited 100% PAP coverage. Moreover, cLTD did not impact astroglia-ASI apposition, but LTP led to selective astroglial withdrawal from large spine synapses. Rats reared in complex environments show increased astroglia-synapse contact (Jones and Greenough, 1996). Meanwhile, greater astroglial apposition can inhibit synapse growth during memory consolidation (Ostroff et al., 2014), and PAP retraction is associated with enhanced fear memory (Badia-Soteras et al., 2023). Together, these findings suggest that non-uniform PAP coverage at dentate gyrus synapses helps fine-tune synaptic efficiency.

In area CA1, PAPs withdraw from synapses following LTP induction, increasing NMDA receptor-dependent extrasynaptic communication without spine-size selectivity (Henneberger et al., 2020). Astroglia also organize synapses into astroglia-defined synaptic clusters (Salmon et al., 2023), and model predictions suggest that processes farther away from synapses are better able to maintain calcium microdomains (Toman et al., 2023). Thin spines are often transient, while larger mushroom-shaped spines are generally more stable, leading to their proposed designations as "learning" and "memory" spines, respectively (Bourne and Harris, 2007). Astroglial withdrawal reduces glutamate uptake (Gavrilov et al., 2018; Henneberger et al., 2020), likely enhancing synaptic transmission (Pannasch et al., 2014). However, it also diminishes the synaptic availability of astroglia-derived D-serine and glycine (Le Bail et al., 2015), potentially impairing further LTP at large spines (Perez-Alvarez et al., 2014), as astrocytic glycine is important for LTP in the dentate MML (Sateesh and Abraham, 2025). Therefore, LTP-associated retraction of astroglial processes from large dentate gyrus synapses may represent a mechanism tailored to this region’s role in pattern separation, possibly enhancing the network contribution of stable “memory” spines (Aimone et al., 2011; Hassanpoor and Saidi, 2020).

Adding complexity to our understanding of tripartite synapses, we found that the PSD center is, on average, ~50 nm from the ASI center. LTP increased PSD offset and the distance between PAP-ASI apposition and the nearest PSD edge, whereas cLTD decreased both. PSD offset showed a stronger positive correlation with ASI area than PSD area. The offset direction was not biased toward or away from astroglia-ASI apposition. Hence, changes in spine rather than PSD size likely contributed to the altered PSD offset during synaptic plasticity. These changes, alongside shifts in PAP proximity, may have shaped astroglial access to the PSD and highlight that astroglial-ASI coverage alone does not fully capture astroglia-synapse dynamics.

Although dentate gyrus astroglia exhibit both functional and morphological diversity (Kosaka and Hama, 1986; Savtchouk et al., 2019; Di Castro and Volterra, 2022; Karpf et al., 2022; Viana et al., 2023), we found no differences between the MML and OML in the proportion of synapses with PAP apposition, nor in the extent of astroglial surround or proximity to the ASI perimeter. The uniform coverage we observed aligns with findings that molecular-layer boundaries do not directly shape astroglial morphology (Bushong et al., 2003) and provides novel ultrastructural evidence that astroglia-synapse relationships are consistent between the MML and OML.

Contrasting Mezey et al. (2004), who reported no difference based on a subset of single EM sections, we found using 3DEM that under control conditions, mean PSD area in the MML was significantly larger than in the OML. Medial perforant path inputs to the MML preferentially exhibit homosynaptic LTP, whereas lateral path inputs to the OML favor LTD (Collitti-Klausnitzer et al., 2021). Still, Hanse and Gustafsson (1992) reported no differences in LTP induction mechanisms or early temporal profiles between these pathways, and total spine density appears consistent across layers (Desmond and Levy, 1985; Gallitano et al., 2016). Direct comparisons of LTD induction between the MML and OML remain limited, although some evidence suggests that the medial and lateral perforant paths differ in their ability to induce heterosynaptic LTD (Doyère et al., 1997). Hence, baseline interlaminar differences are unlikely to account for the LTP- and cLTD-associated changes observed in this study.

In this study, we showed that during LTP and cLTD in the dentate gyrus, PAPs undergo morphological changes that both mirror and diverge from ultrastructural plasticity observed in other brain regions. Astroglial proximity to inhibitory synapses is also dynamic; for example, showing increased apposition in the dorsolateral ventral pallidum following drug-seeking behavior (Kruyer et al., 2022). However, inhibitory synapses are rare in MML and OML, and they exhibit less extensive astroglial coverage (Gavrilov et al., 2018; Yener et al., 2025). Astroglia variability has been demonstrated across sex and developmental stages (Mouton et al., 2002; Conejo et al., 2003; Johnson et al., 2008; Rurak et al., 2022), hence our conclusions are limited to the dentate gyrus of adult, male rat brains. Given the subtlety of the structural changes observed, future studies would benefit from larger sample sizes and the inclusion of both sexes. The efficacy of many astroglial synaptic functions depends on PAP proximity (Pannasch et al., 2014; Toman et al., 2023). Thus, future research should also examine how LTP and cLTD uniquely influence astroglial interactions with the active versus nascent zones—subregions of the PSD distinguished by the presence or absence of apposing presynaptic vesicles. Finally, the dentate gyrus is one of the few regions where adult neurogenesis persists (Aimone et al., 2011; Denoth-Lippuner and Jessberger, 2021). Hence, exploring whether similar PAP coverage between adult-born and pre-existing synapses (Krzisch et al., 2015) is maintained during synaptic plasticity could clarify astroglial contributions to the dentate gyrus memory circuitry.

Data Accessibility

The original EM images, PyReconstruct files (.jser format), and compiled quantitative measurements (in .csv format) used for statistical analysis in R will be made available on 3DEM.org via the Texas Data Repository (doi: https://doi.org/10.18738/T8/S8DT5E).

References

Aboufares El Alaoui A, Jackson M, Fabri M, De Vivo L, Bellesi M (2021) Characterization of subcellular organelles in cortical perisynaptic astrocytes. Front Cell Neurosci 14:573944.

Aimone JB, Deng W, Gage FH (2011) Resolving new memories: a critical look at the dentate gyrus, adult neurogenesis, and pattern separation. Neuron 70:589–596.

Allen NJ, Eroglu C (2017) Cell biology of astrocyte-synapse interactions. Neuron 96:697–708.

Arizono M, Inavalli VVGK, Panatier A, Pfeiffer T, Angibaud J, Levet F, Ter Veer MJT, Stobart J, Bellocchio L, Mikoshiba K, Marsicano G, Weber B, Oliet SHR, Nägerl UV (2020) Structural basis of astrocytic Ca2+ signals at tripartite synapses. Nat Commun 11:1906.

Aten S et al. (2022) Ultrastructural view of astrocyte arborization, astrocyte-astrocyte and astrocyte-synapse contacts, intracellular vesicle-like structures, and mitochondrial network. Prog Neurobiol 213:102264.

Badia-Soteras A, Heistek TS, Kater MSJ, Mak A, Negrean A, Van Den Oever MC, Mansvelder HD, Khakh BS, Min R, Smit AB, Verheijen MHG (2023) Retraction of astrocyte leaflets from the synapse enhances fear memory. Biol Psychiatry 94:226–238.

Batiuk MY, Martirosyan A, Wahis J, De Vin F, Marneffe C, Kusserow C, Koeppen J, Viana JF, Oliveira JF, Voet T, Ponting CP, Belgard TG, Holt MG (2020) Identification of region-specific astrocyte subtypes at single cell resolution. Nat Commun 11:1220.

Bazargani N, Attwell D (2016) Astrocyte calcium signaling: the third wave. Nat Neurosci 19:182–189.

Bellesi M, De Vivo L, Tononi G, Cirelli C (2015) Effects of sleep and wake on astrocytes: clues from molecular and ultrastructural studies. BMC Biol 13:66.

Bernardinelli Y, Randall J, Janett E, Nikonenko I, König S, Jones EV, Flores CE, Murai KK, Bochet CG, Holtmaat A, Muller D (2014) Activity-dependent structural plasticity of perisynaptic astrocytic domains promotes excitatory synapse stability. Curr Biol 24:1679–1688.

Bindocci E, Savtchouk I, Liaudet N, Becker D, Carriero G, Volterra A (2017) Three-dimensional Ca2+ imaging advances understanding of astrocyte biology. Science 356:eaai8185.

Bourne J, Harris KM (2007) Do thin spines learn to be mushroom spines that remember? Curr Opin Neurobiol 17:381–386.

Bowden JB, Abraham WC, Harris KM (2012) Differential effects of strain, circadian cycle, and stimulation pattern on LTP and concurrent LTD in the dentate gyrus of freely moving rats. Hippocampus 22:1363–1370.

Bromer C, Bartol TM, Bowden JB, Hubbard DD, Hanka DC, Gonzalez PV, Kuwajima M, Mendenhall JM, Parker PH, Abraham WC, Sejnowski TJ, Harris KM (2018) Long-term potentiation expands information content of hippocampal dentate gyrus synapses. Proc Natl Acad Sci 115 Available at: https://pnas.org/doi/full/10.1073/pnas.1716189115 [Accessed February 29, 2024].

Bushong EA, Martone ME, Ellisman MH (2003) Examination of the relationship between astrocyte morphology and laminar boundaries in the molecular layer of adult dentate gyrus. J Comp Neurol 462:241–251.

Cardona A, Saalfeld S, Schindelin J, Arganda-Carreras I, Preibisch S, Longair M, Tomancak P, Hartenstein V, Douglas RJ (2012) TrakEM2 software for neural circuit reconstruction Samuel A, ed. PLoS ONE 7:e38011.

Chai H, Diaz-Castro B, Shigetomi E, Monte E, Octeau JC, Yu X, Cohn W, Rajendran PS, Vondriska TM, Whitelegge JP, Coppola G, Khakh BS (2017) Neural circuit-specialized astrocytes: transcriptomic, proteomic, morphological, and functional evidence. Neuron 95:531-549.e9.

Chipman PH, Fung CCA, Pazo Fernandez A, Sawant A, Tedoldi A, Kawai A, Ghimire Gautam S, Kurosawa M, Abe M, Sakimura K, Fukai T, Goda Y (2021) Astrocyte GluN2C NMDA receptors control basal synaptic strengths of hippocampal CA1 pyramidal neurons in the stratum radiatum. eLife 10:e70818.

Chung W-S, Allen NJ, Eroglu C (2015) Astrocytes control synapse formation, function, and elimination. Cold Spring Harb Perspect Biol 7:a020370.

Collitti-Klausnitzer J, Hagena H, Dubovyk V, Manahan-Vaughan D (2021) Preferential frequency-dependent induction of synaptic depression by the lateral perforant path and of synaptic potentiation by the medial perforant path inputs to the dentate gyrus. Hippocampus 31:957–981.

Conejo NM, González-Pardo H, Pedraza C, Navarro FF, Vallejo G, Arias JL (2003) Evidence for sexual difference in astrocytes of adult rat hippocampus. Neurosci Lett 339:119–122.

Denizot A, Arizono M, Nägerl UV, Berry H, De Schutter E (2022) Control of Ca^{2+} signals by astrocyte nanoscale morphology at tripartite synapses. Glia 70:2378–2391.

Denoth-Lippuner A, Jessberger S (2021) Formation and integration of new neurons in the adult hippocampus. Nat Rev Neurosci 22:223–236.

Desmond NL, Levy WB (1985) Granule cell dendritic spine density in the rat hippocampus varies with spine shape and location. Neurosci Lett 54:219–224.

Di Castro MA, Volterra A (2022) Astrocyte control of the entorhinal cortex-dentate gyrus circuit: Relevance to cognitive processing and impairment in pathology. Glia 70:1536–1553.

Doyère V, Srebro B, Laroche S (1997) Heterosynaptic LTD and Depotentiation in the Medial Perforant Path of the Dentate Gyrus in the Freely Moving Rat. J Neurophysiol 77:571–578.

Durkee C, Kofuji P, Navarrete M, Araque A (2021) Astrocyte and neuron cooperation in long-term depression. Trends Neurosci 44:837–848.

Endo F, Kasai A, Soto JS, Yu X, Qu Z, Hashimoto H, Gradinaru V, Kawaguchi R, Khakh BS (2022) Molecular basis of astrocyte diversity and morphology across the CNS in health and disease. Science 378:eadc9020.

Fiacco TA, McCarthy KD (2018) Multiple lines of evidence indicate that gliotransmission does not occur under physiological conditions. J Neurosci 38:3–13.

Fiala JC (2005) Reconstruct: a free editor for serial section microscopy. J Microsc 218:52–61.

Fiala JC, Harris KM (2001a) Cylindrical diameters method for calibrating section thickness in serial electron microscopy. J Microsc 202:468–472.

Fiala JC, Harris KM (2001b) Extending unbiased stereology of brain ultrastructure to three-dimensional volumes. J Am Med Inform Assoc 8:1–16.

Gallitano AL, Satvat E, Gil M, Marrone DF (2016) Distinct dendritic morphology across the blades of the rodent dentate gyrus. Synapse 70:277–282.

Gavrilov N, Golyagina I, Brazhe A, Scimemi A, Turlapov V, Semyanov A (2018) Astrocytic coverage of dendritic spines, dendritic shafts, and axonal Boutons in hippocampal neuropil. Front Cell Neurosci 12:248.

Genoud C, Quairiaux C, Steiner P, Hirling H, Welker E, Knott GW (2006) Plasticity of astrocytic coverage and glutamate transporter expression in adult mouse cortex Stevens C, ed. PLoS Biol 4:e343.

Hainmueller T, Bartos M (2020) Dentate gyrus circuits for encoding, retrieval and discrimination of episodic memories. Nat Rev Neurosci 21:153–168.

Hanse E, Gustafsson B (1992) Long-term Potentiation and Field EPSPs in the Lateral and Medial Perforant Paths in the Dentate Gyrus *In Vitro*: a Comparison. Eur J Neurosci 4:1191–1201.

Harris K, Stevens J (1989) Dendritic spines of CA 1 pyramidal cells in the rat hippocampus: serial electron microscopy with reference to their biophysical characteristics. J Neurosci 9:2982–2997.

Harris KM, Hubbard DD, Kuwajima M, Abraham WC, Bourne JN, Bowden JB, Haessly A, Mendenhall JM, Parker PH, Shi B, Spacek J (2022) Dendritic spine density scales with microtubule number in rat hippocampal dendrites. Neuroscience 489:84–97.

Harris KM, Perry E, Bourne J, Feinberg M, Ostroff L, Hurlburt J (2006) Uniform serial sectioning for transmission electron microscopy. J Neurosci 26:12101–12103.

Harris KM, Spacek J, Bell ME, Parker PH, Lindsey LF, Baden AD, Vogelstein JT, Burns R (2015) A resource from 3D electron microscopy of hippocampal neuropil for user training and tool development. Sci Data 2:150046.

Harris KM, Weinberg RJ (2012) Ultrastructure of synapses in the mammalian brain. Cold Spring Harb Perspect Biol 4:a005587–a005587.

Hassanpoor H, Saidi M (2020) An investigation into the effective role of astrocyte in the hippocampus pattern separation process: A computational modeling study. J Theor Biol 487:110114.

Henneberger C et al. (2020) LTP induction boosts glutamate spillover by driving withdrawal of perisynaptic astroglia. Neuron 108:919-936.e11.

Henneberger C, Papouin T, Oliet SHR, Rusakov DA (2010) Long-term potentiation depends on release of d-serine from astrocytes. Nature 463:232–236.

Hirrlinger J, Hülsmann S, Kirchhoff F (2004) Astroglial processes show spontaneous motility at active synaptic terminals *in situ*. Eur J Neurosci 20:2235–2239.

Johnson RT, Breedlove SM, Jordan CL (2008) Sex differences and laterality in astrocyte number and complexity in the adult rat medial amygdala. J Comp Neurol 511:599–609.

Jones TA, Greenough WT (1996) Ultrastructural Evidence for Increased Contact between Astrocytes and Synapses in Rats Reared in a Complex Environment. Neurobiol Learn Mem 65:48–56.

Kalimo H (1976) The role of the blood-brain barrier in perfusion fixation of the brain for electron microscopy. Histochem J 8:1–12.

Karpf J, Unichenko P, Chalmers N, Beyer F, Wittmann M-T, Schneider J, Fidan E, Reis A, Beckervordersandforth J, Brandner S, Liebner S, Falk S, Sagner A, Henneberger C, Beckervordersandforth R (2022) Dentate gyrus astrocytes exhibit layer-specific molecular, morphological and physiological features. Nat Neurosci 25:1626–1638.

Kinney JP, Spacek J, Bartol TM, Bajaj CL, Harris KM, Sejnowski TJ (2013) Extracellular sheets and tunnels modulate glutamate diffusion in hippocampal neuropil. J Comp Neurol 521:448–464.

Kirov SA, Sorra KE, Harris KM (1999) Slices have more synapses than perfusion-fixed hippocampus from both young and mature rats. J Neurosci 19:2876–2886.

Kleinjan MS, Buchta WC, Ogelman R, Hwang I-W, Kuwajima M, Hubbard DD, Kareemo DJ, Prikhodko O, Olah SL, Gomez Wulschner LE, Abraham WC, Franco SJ, Harris KM, Oh WC, Kennedy MJ (2023) Dually innervated dendritic spines develop in the absence of excitatory activity and resist plasticity through tonic inhibitory crosstalk. Neuron 111:362-371.e6.

Korogod N, Petersen CC, Knott GW (2015) Ultrastructural analysis of adult mouse neocortex comparing aldehyde perfusion with cryo fixation. eLife 4:e05793.

Kosaka T, Hama K (1986) Three-dimensional structure of astrocytes in the rat dentate gyrus. J Comp Neurol 249:242–260.

Kruyer A, Dixon D, Angelis A, Amato D, Kalivas PW (2022) Astrocytes in the ventral pallidum extinguish heroin seeking through GAT-3 upregulation and morphological plasticity at D1-MSN terminals. Mol Psychiatry 27:855–864.

Krzisch M, Temprana SG, Mongiat LA, Armida J, Schmutz V, Virtanen MA, Kocher-Braissant J, Kraftsik R, Vutskits L, Conzelmann K-K, Bergami M, Gage FH, Schinder AF, Toni N (2015) Pre-existing astrocytes form functional perisynaptic processes on neurons generated in the adult hippocampus. Brain Struct Funct 220:2027–2042.

Kuwajima M, Mendenhall JM, Harris KM (2013a) Large-volume reconstruction of brain tissue from high-resolution serial section images acquired by SEM-based scanning transmission electron microscopy. In: Nanoimaging (Sousa AA, Kruhlak MJ, eds), pp 253–273 Methods in Molecular Biology. Totowa, NJ: Humana Press. Available at: https://link.springer.com/10.1007/978-1-62703-137-0_15 [Accessed November 23, 2024].

Kuwajima M, Mendenhall JM, Lindsey LF, Harris KM (2013b) Automated Transmission-Mode Scanning Electron Microscopy (tSEM) for Large Volume Analysis at Nanoscale Resolution Fox MA, ed. PLoS ONE 8:e59573.

Kuznetsova A, Brockhoff PB, Christensen RHB (2017) lmerTest package: Tests in linear mixed effects models. J Stat Softw 82 Available at: http://www.jstatsoft.org/v82/i13/ [Accessed November 25, 2024].

Lanjakornsiripan D, Pior B-J, Kawaguchi D, Furutachi S, Tahara T, Katsuyama Y, Suzuki Y, Fukazawa Y, Gotoh Y (2018) Layer-specific morphological and molecular differences in neocortical astrocytes and their dependence on neuronal layers. Nat Commun 9:1623.

Le Bail M, Martineau M, Sacchi S, Yatsenko N, Radzishevsky I, Conrod S, Ait Ouares K, Wolosker H, Pollegioni L, Billard J-M, Mothet J-P (2015) Identity of the NMDA receptor coagonist is synapse specific and developmentally regulated in the hippocampus. Proc

Natl Acad Sci 112 Available at: https://pnas.org/doi/full/10.1073/pnas.1416668112 [Accessed April 20, 2025].

Lee CT, Laughlin JG, Angliviel De La Beaumelle N, Amaro RE, McCammon JA, Ramamoorthi R, Holst M, Rangamani P (2020) 3D mesh processing using GAMer 2 to enable reaction-diffusion simulations in realistic cellular geometries Berry H, ed. PLOS Comput Biol 16:e1007756.

Lee J-H, Kim J, Noh S, Lee H, Lee SY, Mun JY, Park H, Chung W-S (2021) Astrocytes phagocytose adult hippocampal synapses for circuit homeostasis. Nature 590:612–617.

Letellier M, Goda Y (2023) Astrocyte Calcium Signaling Shifts the Polarity of Presynaptic Plasticity. Neuroscience 525:38–46.

Letellier M, Park YK, Chater TE, Chipman PH, Gautam SG, Oshima-Takago T, Goda Y (2016) Astrocytes regulate heterogeneity of presynaptic strengths in hippocampal networks. Proc Natl Acad Sci 113 Available at: https://pnas.org/doi/full/10.1073/pnas.1523717113 [Accessed April 3, 2025].

Lim D, Semyanov A, Genazzani A, Verkhratsky A (2021) Calcium signaling in neuroglia. In: International Review of Cell and Molecular Biology, pp 1–53. Elsevier. Available at: https://linkinghub.elsevier.com/retrieve/pii/S1937644821000034 [Accessed November 11, 2024].

Liu J-H, Zhang M, Wang Q, Wu D-Y, Jie W, Hu N-Y, Lan J-Z, Zeng K, Li S-J, Li X-W, Yang J-M, Gao T-M (2022) Distinct roles of astroglia and neurons in synaptic plasticity and memory. Mol Psychiatry 27:873–885.

Medvedev N, Popov V, Henneberger C, Kraev I, Rusakov DA, Stewart MG (2014) Glia selectively approach synapses on thin dendritic spines. Philos Trans R Soc B Biol Sci 369:20140047.

Mezey S, Doyère V, De Souza I, Harrison E, Cambon K, Kendal CE, Davies H, Laroche S, Stewart MG (2004) Long-term synaptic morphometry changes after induction of long-term potentiation and long-term depression in the dentate gyrus of awake rats are not simply mirror phenomena. Eur J Neurosci 19:2310–2318.

Mouton PR, Long JM, Lei D-L, Howard V, Jucker M, Calhoun ME, Ingram DK (2002) Age and gender effects on microglia and astrocyte numbers in brains of mice. Brain Res 956:30–35.

Okamoto K-I, Nagai T, Miyawaki A, Hayashi Y (2004) Rapid and persistent modulation of actin dynamics regulates postsynaptic reorganization underlying bidirectional plasticity. Nat Neurosci 7:1104–1112.

Ostroff LE, Manzur MK, Cain CK, Ledoux JE (2014) Synapses lacking astrocyte appear in the amygdala during consolidation of pavlovian threat conditioning. J Comp Neurol 522:2152–2163.

Pannasch U, Freche D, Dallérac G, Ghézali G, Escartin C, Ezan P, Cohen-Salmon M, Benchenane K, Abudara V, Dufour A, Lübke JHR, Déglon N, Knott G, Holcman D, Rouach N (2014) Connexin 30 sets synaptic strength by controlling astroglial synapse invasion. Nat Neurosci 17:549–558.

Perez-Alvarez A, Navarrete M, Covelo A, Martin ED, Araque A (2014) Structural and functional plasticity of astrocyte processes and dendritic spine interactions. J Neurosci 34:12738–12744.

Reynolds ES (1963) The use of lead citrate at high pH as an electron-opaque stain in electron microscopy. J Cell Biol 17:208–212.

Risher WC, Patel S, Kim IH, Uezu A, Bhagat S, Wilton DK, Pilaz L-J, Singh Alvarado J, Calhan OY, Silver DL, Stevens B, Calakos N, Soderling SH, Eroglu C (2014) Astrocytes refine cortical connectivity at dendritic spines. eLife 3:e04047.

Rurak GM, Simard S, Freitas-Andrade M, Lacoste B, Charih F, Van Geel A, Stead J, Woodside B, Green JR, Coppola G, Salmaso N (2022) Sex differences in developmental patterns of neocortical astroglia: A mouse translatome database. Cell Rep 38:110310.

Rusakov DA (2015) Disentangling calcium-driven astrocyte physiology. Nat Rev Neurosci 16:226–233.

Saalfeld S, Fetter R, Cardona A, Tomancak P (2012) Elastic volume reconstruction from series of ultra-thin microscopy sections. Nat Methods 9:717–720.

Sahlender DA, Savtchouk I, Volterra A (2014) What do we know about gliotransmitter release from astrocytes? Philos Trans R Soc B Biol Sci 369:20130592.

Saint-Martin M, Goda Y (2023) Astrocyte–synapse interactions and cell adhesion molecules. FEBS J 290:3512–3526.

Salmon CK, Syed TA, Kacerovsky JB, Alivodej N, Schober AL, Sloan TFW, Pratte MT, Rosen MP, Green M, Chirgwin-Dasgupta A, Mehta S, Jilani A, Wang Y, Vali H, Mandato CA, Siddiqi K, Murai KK (2023) Organizing principles of astrocytic nanoarchitecture in the mouse cerebral cortex. Curr Biol:S0960982223000775.

Sateesh S, Abraham WC (2025) Differential Astrocyte-supplied NMDAR Co-Agonist for CA1 versus Dentate Gyrus Long-term Potentiation. Available at: http://biorxiv.org/lookup/doi/10.1101/2025.05.05.652314 [Accessed May 12, 2025].

Savtchouk I, Di Castro MA, Ali R, Stubbe H, Luján R, Volterra A (2019) Circuit-specific control of the medial entorhinal inputs to the dentate gyrus by atypical presynaptic NMDARs activated by astrocytes. Proc Natl Acad Sci 116:13602–13610.

Schindelin J, Arganda-Carreras I, Frise E, Kaynig V, Longair M, Pietzsch T, Preibisch S, Rueden C, Saalfeld S, Schmid B, Tinevez J-Y, White DJ, Hartenstein V, Eliceiri K, Tomancak P, Cardona A (2012) Fiji: an open-source platform for biological-image analysis. Nat Methods 9:676–682.

Semyanov A, Verkhratsky A (2021) Astrocytic processes: from tripartite synapses to the active milieu. Trends Neurosci 44:781–792.

Shigetomi E, Bushong EA, Haustein MD, Tong X, Jackson-Weaver O, Kracun S, Xu J, Sofroniew MV, Ellisman MH, Khakh BS (2013) Imaging calcium microdomains within entire astrocyte territories and endfeet with GCaMPs expressed using adeno-associated viruses. J Gen Physiol 141:633–647.

Tan CX, Burrus Lane CJ, Eroglu C (2021) Role of astrocytes in synapse formation and maturation. In: Current Topics in Developmental Biology, pp 371–407. Elsevier. Available at: https://linkinghub.elsevier.com/retrieve/pii/S0070215320301435 [Accessed November 11, 2024].

Toman M, Wade JJ, Verkhratsky A, Dallas M, Bithell A, Flanagan B, Harkin J, McDaid L (2023) The influence of astrocytic leaflet motility on ionic signalling and homeostasis at active synapses. Sci Rep 13:3050.

Tønnesen J, Inavalli VVGK, Nägerl UV (2018) Super-resolution imaging of the extracellular space in living brain tissue. Cell 172:1108-1121.e15.

Ventura R, Harris KM (1999) Three-dimensional relationships between hippocampal synapses and astrocytes. J Neurosci 19:6897–6906.

Viana JF, Machado JL, Abreu DS, Veiga A, Barsanti S, Tavares G, Martins M, Sardinha VM, Guerra-Gomes S, Domingos C, Pauletti A, Wahis J, Liu C, Calì C, Henneberger C, Holt MG, Oliveira JF (2023) Astrocyte structural heterogeneity in the mouse hippocampus. Glia 71:1667–1682.

Villa KL, Berry KP, Subramanian J, Cha JW, Oh WC, Kwon H-B, Kubota Y, So PTC, Nedivi E (2016) Inhibitory synapses are repeatedly assembled and removed at persistent sites in vivo. Neuron 89:756–769.

Wenzel J, Lammert G, Meyer U, Krug M (1991) The influence of long-term potentiation on the spatial relationship between astrocyte processes and potentiated synapses in the dentate gyrus neuropil of rat brain. Brain Res 560:122–131.

Wetzel AW, Bakal J, Dittrich M, Hildebrand DGC, Morgan JL, Lichtman JW (2016) Registering large volume serial-section electron microscopy image sets for neural circuit reconstruction using FFT signal whitening. In: 2016 IEEE Applied Imagery Pattern Recognition Workshop (AIPR), pp 1–10. Washington, DC, USA: IEEE. Available at: http://ieeexplore.ieee.org/document/8010595/ [Accessed November 25, 2024].

Witcher MR, Kirov SA, Harris KM (2007) Plasticity of perisynaptic astroglia during synaptogenesis in the mature rat hippocampus. Glia 55:13–23.

Yener Y, Motta A, Helmstaedter M (2025) Connectomic analysis of astrocyte-synapse interactions in the cerebral cortex. Available at: http://biorxiv.org/lookup/doi/10.1101/2025.02.20.639274 [Accessed April 3, 2025].

Zhou Q, Homma KJ, Poo M (2004) Shrinkage of dendritic spines associated with long-term depression of hippocampal synapses. Neuron 44:749–757.

Figure Legends

Figure 1. **LTP and cLTD outcomes and preparation of dentate gyrus MML and OML tissue for 3DEM. A - D**: Experimental hemisphere medial perforant pathway (MPP) responses (red, LTP), control hemisphere MPP responses (blue, control), and experimental hemisphere lateral perforant pathway (LPP) responses (green, cLTD). **(A)** Graphs of percent change in average fEPSP response relative to baseline for (A) animals 1, 2, and 5 sacrificed 30 minutes (min) after DBS stimulation (delivered over t = 0-10 mins), and **(B)** animals 3, 4, and 6 sacrificed 2 hours (h) after DBS stimulation (delivered over t = 0-10 mins). **(C)** Representative smoothed waveforms obtained during the times shown as gray vertical bars in the graphs of A and B for animals 1-6. Pre-DBS baseline responses (blue, dotted) are superimposed by post-DBS responses (solid). Scale bars: 5 mV (vertical), 5 ms (horizontal). **(D)** (Left) Example parasagittal hippocampal tissue section with visible tract from recording electrode positioned in dentate gyrus hilus (top) and adjacent tissue section used for EM series preparation (bottom). (Middle) Region of dentate gyrus molecular layer isolated for ultra-thin serial sectioning. Horizontal lines indicate sectioning planes: OML (grey) and MML (black) at 250 µm and 125 µm from top of granule cell layer, respectively. OML and MML were sectioned separately for animals 1-4 (d_i), and on the same tissue section for animals 5 and 6 (white sectioning plane, $\alpha = 26.6^{\circ}$, d_{ii}). (Right) Stacks of 200-300 serial section EM images were obtained in the OML (top) and MML (bottom) using transmission electron microscopy or scanning electron microscopy operating in the transmission mode. Scale bars: 500 µm.

Figure 2. **Automated ASI detection and measurement of astroglia apposition at the ASI perimeter.** **(A)** EM image of serial section (S) 38 and (B) corresponding 3D reconstruction showing the postsynaptic dendritic spine (sp, yellow), presynaptic axon (ax, dark blue), perisynaptic astroglia (ag, light blue), and postsynaptic density (PSD, red). The ASI perimeter (peri) is indicated in orange (diamonds, A; outline, B). **(C)** Detection of ASI facets (black triangles, f_{ai}) on the axon mesh surface with normal vector projections (orange lines/arrow) from the center of each triangular mesh facet (black dot) to the intersecting spine mesh facet (f_{si}). (Right) Zoomed-in view of an example ASI face highlighted with bold black edges and maximum d_{ASI}. **(D)** ASI axon facets with corresponding normal vectors (orange). **(E)** Relative location of PSD within the ASI (brown) projected onto the axon surface and **(F)** the spine surface. The computed ASI perimeter, ASI centroid (white star), and PSD centroid (white diamond) are shown. For this synapse the centroid ends up in the middle of the perforation. **(G)** Concentric rings around the ASI perimeter indicate the Euclidean distances between the astroglia and ASI perimeter (d_{ag}). Rings are color-coded by astroglia presence (ag+, green) or absence (ag-, red) within a particular d_{ag}. The axon and surrounding astroglia are also shown. (Inset) Zoomed-in view of distance thresholds ($d_{ag} \leq$ 10-120 nm) tested. **(H)** Zoomed-in view of EM image from A, showing astroglia positioned 10 nm from the ASI perimeter (orange diamond) at one edge (d_{ag} = 10 nm) but 140 nm away at the opposite edge (d_{ag}>120 nm, exceeding the maximum distance threshold tested), with an intervening axon. **(I)** EM image of a different synapse on the same dendrite as in A, observed on S42, depicting d_{ag} = 30 nm. In H and I, insets show an enlarged view of the regions indicated by white boxes. **(J)** Length of the ASI perimeter apposed (ag+, green) and not apposed (ag-, red) by astroglia based on $d_{ag} \leq$ 10 nm (left), 30 nm (middle), and 120 nm (right). The axon and surrounding astroglia are also shown. The same synapse is shown in A-H and J, with consistent color coding applied across all panels. Scale bars, scale cube edge lengths: 250 nm.

Figure 3. Nearly all MML spines have some perisynaptic astroglia and undergo a sustained increase in spine volume and ASI length during LTP relative to control stimulation. (A) EM image (left) and 3D reconstruction (right) of the spine (sp, yellow), postsynaptic density (PSD, red), presynaptic axon (ax, dark blue), and perisynaptic astroglia (ag, light blue) for an MML synapse during control (con, top) and LTP (bottom) at 30 min and **(B)** 2 h after LTP induction. The ASI perimeter is indicated by orange diamonds in EM images (A-B). **(C)** Synapse categories based on astroglial presence (ASI^{ag+}) or absence (ASI^{ag-}) within 120 nm of the ASI perimeter and specific astroglia location. The spine, axon, PSD, perisynaptic astroglia, presynaptic vesicles (small white circles), and ASI (brown oval) are represented using the same color scheme as A-B. Panels D-G show data from control (blue) and LTP (red) MML synapses at 30 min (left) and 2 h (right) during LTP. **(D)** Bar graph of overall synapse percentage in each synapse category. Numbers below bars indicate synapse count. Dots represent dendrite-specific synapse percentages. (Insets) Line plots show ASI^{ag+} synapse percentages based on each d_{ag} threshold tested. **(E)** Kernel density estimate plots show the probability density functions (PDFs) for spine volume (log-scale axis) and **(F)** ASI perimeter (square-root axis) for synapse subsets based on d_{ag}. Synapse counts color-coded by condition are shown in bottom left corner in E and apply to E-F (relatively few synapses in cluster 2 had $d_{ag} \leq 10$ nm). **(G)** Regression plot of spine volume (log-scale y-axis) and ASI perimeter (square-root x-axis) for synapses in cluster 1 (c1) or cluster 2 (c2) with $d_{ag} \leq 10$ (lowest opacity), 30 nm (medium opacity), and 120 nm (highest opacity). Raw data, R^2 values, and Benjamini-Hochberg (BH)-adjusted p-values (condition effect) for $d_{ag} \leq 120$ nm are displayed. Synapse counts color-coded by condition are shown in bottom right corner. Asterisks indicate significant condition effects for synapse subsets defined by d_{ag} (BH-adjusted $^{**}p < 0.01$, $^{***}p < 0.001$; see Table S1 for statistical details). Scale bar and cube (edge length = 250 nm) in A apply to A-B.

Figure 4. The PSD area range expands, and the PSD offset from the ASI center increases during LTP. (A) 3D reconstruction of the postsynaptic density (PSD, red) projected onto the axon mesh (ax, dark blue), perisynaptic astroglia (ag, light blue), ASI perimeter color-coded by presence (ag+, green) or absence (ag-, red) of astroglia within 120 nm, ASI centroid (white star), and PSD centroid (white diamond) for an MML synapse during control (top) and LTP (bottom) at 30 min and **(B)** 2 h following LTP induction. **(C)** Kernel density estimate (KDE) plots show the probability density function (PDF) for PSD area (log-scale axis) and **(D)** PSD offset from the ASI center (log-scale axis) for synapses subset based on d_{ag}. **(E)** Regression plot of PSD area (log-scale y-axis) and **(F)** PSD offset from the ASI center (log-scale y-axis) versus ASI area (log-scale x-axis) for c1 or c2 synapses with $d_{ag} \leq 10$ nm (lowest opacity lines), 30 nm (medium opacity lines), and 120 nm (highest opacity lines). Raw data, R^2 values, and Benjamini-Hochberg (BH)-adjusted p-values (condition effect) for $d_{ag} \leq 120$ nm are displayed. In C-F, data are from control (blue) and LTP (red) MML synapses at 30 min (left) and 2 h (right) during LTP (see Figure 3G for synapse counts). Asterisks indicate significant condition and condition-by-ASI perimeter interaction (int) effects for synapse subsets defined by d_{ag} (BH-adjusted $*p < 0.05$, $**p < 0.01$; see Table S1 for statistical details). Scale cube (edge length = 100 nm) in A applies to A-B. Cluster legend in E applies to E-F.

Figure 5. By 2 hours during LTP, PAP coverage length is reduced, and the minimum PAP distance to the ASI perimeter is increased selectively at large synapses. Meanwhile, astroglial access to the PSD decreases across synapse sizes. (A) Schematic representation of the ASI perimeter (orange) and the segment of its length (l_{ag}, green) surrounded by perisynaptic astroglia (ag, light blue) within a given distance threshold (d_{ag}, dashed black lines), with key synaptic structures (spine, yellow; PSD, red) also indicated. **(B)** Regression plot of l_{ag} (square-root y-axis) versus ASI perimeter (square-root x-axis) for c1 and c2 synapses with $d_{ag} \leq 120$ nm at 30 min and **(C)** 2 h during LTP. In B-C, l_{ag} was measured using d_{ag} thresholds of ≤ 10 nm (lowest opacity lines), 30 nm (medium opacity), and 120 nm (highest opacity). Raw data, R² values, and Benjamini-Hochberg (BH)-adjusted p-values (condition effect) for $d_{ag} \leq 120$ nm are displayed. All subsequent regression plots in (E-F, I-J) were performed separately for c1 and c2 synapses with $d_{ag} \leq 10$, 30, and 120 nm, using the same marker and opacity scheme as in B-C, with statistical results displayed similarly. **(D)** Illustration of the average distance (black d_{ag} arrow) from the ASI perimeter to the nearest astroglial process, using the same schematic elements as in A. **(E)** Regression plot of average d_{ag} (log-scale y-axis) versus ASI perimeter (square-root x-axis) at 30 min and (**F**) 2 h. **(G)** Illustration of the average distance from astroglia-apposed ASI perimeter (within 120 nm) to the nearest PSD edge (black $d_{agASI\text{-}PSD}$ arrow), using the same schematic elements as in A. **(H)** Kernel density plots of average $d_{agASI\text{-}PSD}$ (log-scale y-axis) for synapses grouped by d_{ag} at 30 min (left) and 2 h (right). **(I)** Regression plot of average $d_{agASI\text{-}PSD}$ (log-scale y-axis) versus average distance from all ASI perimeter vertices to the nearest PSD edge ($d_{ASI\text{-}PSD}$, log-scale x-axis), and (**J**) ASI area (log-scale x-axis), at 30 min (left) and 2 h (right). In all plots (B-C, E-F, H-J), data are shown for control (blue) and LTP (red) synapses (see Figure 3G for synapse counts). Asterisks indicate significant condition effects for synapse subsets defined by d_{ag} (BH-

adjusted $*p < 0.05$, $**p < 0.01$, $***p < 0.001$; see Table S1 for statistical details). Cluster legend in B applies to B-C, E-F, I-J.

Figure 6. Nearly all OML spines have some perisynaptic astroglia and undergo a transient decrease in ASI perimeter length during cLTD relative to control stimulation. (A) EM image (left) and 3D reconstruction (right) of the spine (sp, yellow), postsynaptic density (PSD, red), presynaptic axon (ax, dark blue), and perisynaptic astroglia (ag, light blue) for an OML synapse during control (top) and cLTD (bottom) at 30 min and **(B)** 2 h after cLTD induction. The ASI perimeter is indicated by orange diamonds in EM images (A-B). **(C)** Synapse categories based on astroglial presence (ASI^{ag+}) or absence (ASI^{ag-}) within 120 nm of the ASI perimeter and specific astroglia location. The spine, axon, PSD, perisynaptic astroglia, presynaptic vesicles (small white circles), and ASI (brown oval) are represented using same color scheme as A-B. Panels D-G show data from control (blue) and cLTD (green) OML synapses at 30 min (left) and 2 h (right) during cLTD. **(D)** Bar graph of overall synapse percentage in each synapse category. Numbers below bars indicate synapse count. Dots represent dendrite-specific synapse percentages. (Insets) Line plots show ASI^{ag+} synapse percentages based on each d_{ag} threshold tested. **(E)** Kernel density estimate plots show the probability density functions for spine volume (log-scale axis) and **(F)** ASI perimeter (square-root axis) for synapse subsets based on d_{ag} (*$p < 0.01$ that control and cLTD distributions differ). Synapse counts color-coded by condition are shown in bottom left corner in E and apply to E-F. **(G)** Regression plot of spine volume (log-scale y-axis) and ASI perimeter (square-root x-axis) for c1 or c2 synapses with $d_{ag} \leq 10$ nm (lowest opacity), 30 nm (medium opacity), and 120 nm (highest opacity). Raw data, R^2 values, and Benjamini-Hochberg (BH)-adjusted p-values (condition effect) for $d_{ag} \leq 120$ nm are displayed. Synapse counts color-coded by condition are shown in bottom right corner (relatively few synapses in cluster 2 had $d_{ag} \leq 10$ nm). Asterisks indicate significant condition effects for synapse subsets defined by d_{ag} (BH-adjusted *$p < 0.05$; see Table S1 for statistical details). Scale bar and cube (edge length = 250 nm) in A apply to A-B.

Figure 7. The PSD area does not change, but the PSD offset from the ASI center transiently decreases during cLTD. (A) 3D reconstruction of the postsynaptic density (PSD, red) projected onto the axon mesh (ax, dark blue), perisynaptic astroglia (ag, light blue), ASI perimeter color coded by presence (ag+, green) or absence (ag-, red) of astroglia within 120 nm, ASI centroid (white star), and PSD centroid (white diamond) for an OML synapse during control (top) and cLTD (bottom) at 30 min and **(B)** 2 h following cLTD induction. **(C)** Kernel density estimate (KDE) plots show the probability density function (PDF) for PSD area (log-scale axis) and **(D)** PSD offset from the ASI center (log-scale axis) for synapses subset based on d_{ag}. **(E)** Regression plot of PSD area (log-scale y-axis) and **(F)** PSD offset from the ASI center (log-scale y-axis) versus ASI area (log-scale x-axis) for c1 or c2 synapses with $d_{ag} \leq 10$ nm (lowest opacity lines), 30 nm (medium opacity lines), and 120 nm (highest opacity lines). Raw data, R^2 values, and Benjamini-Hochberg (BH)-adjusted p-values (condition effect) for $d_{ag} \leq 120$ nm are displayed. In C-F, data are from control (blue) and cLTD (green) OML synapses at 30 min (left) and 2 h (right) during cLTD (see Figure 6G for synapse counts). Asterisks indicate significant condition and condition-by-ASI perimeter interaction (int) effects for synapse subsets defined by d_{ag} (BH-adjusted $^*p < 0.05$, $^{**}p < 0.01$, $^{***}p < 0.001$; see Table S1 for statistical details). Scale cube (edge length = 100 nm) in A applies to A-B. Cluster legend in E applies to E-F.

Figure 8. **During cLTD, there is a minimal change in PAP coverage length and minimum distance to the ASI perimeter, but a transient increase in astroglial access to the PSD.** **(A)** Schematic representation of the ASI perimeter (orange) and the segment of its length (l_{ag}, green) surrounded by perisynaptic astroglia (light blue) within a given distance threshold (d_{ag}, dashed black lines), with key synaptic structures (spine, yellow; PSD, red) also indicated. **(B)** Regression plot of l_{ag} (square-root y-axis) versus ASI perimeter (square-root x-axis) for c1 and c2 synapses with $d_{ag} \leq 120$ nm at 30 min and **(C)** 2 h during cLTD. In B-C, l_{ag} was measured using d_{ag} thresholds of ≤ 10 nm (lowest opacity lines), 30 nm (medium opacity), and 120 nm (highest opacity). Raw data, R^2 values, and Benjamini-Hochberg (BH)-adjusted p-values (condition effect) for $d_{ag} \leq 120$ nm are displayed. All subsequent regression plots in (E-F, I-J) were performed separately for c1 and c2 synapses with $d_{ag} \leq 10$, 30, and 120 nm, using the same marker and opacity scheme as in B-C, with statistical results displayed similarly. **(D)** Illustration of the average distance (black d_{ag} arrow) from the ASI perimeter to the nearest astroglial process, using the same schematic elements as in A. **(E)** Regression plot of average d_{ag} (log-scale y-axis) versus ASI perimeter (square-root x-axis) at 30 min and **(F)** 2 h. **(G)** Illustration of the average distance from astroglia-apposed ASI perimeter (within 120 nm) to the nearest PSD edge (black $d_{agASI\text{-}PSD}$ arrow), using the same schematic elements as in A. **(H)** Kernel density plots of average $d_{agASI\text{-}PSD}$ (log-scale y-axis) for synapses grouped by d_{ag} at 30 min (left) and 2 h (right). **(I)** Regression plot of average $d_{agASI\text{-}PSD}$ (log-scale y-axis) versus average distance from all ASI perimeter vertices to the nearest PSD edge ($d_{ASI\text{-}PSD}$, log-scale x-axis), and (**J**) ASI area (log-scale x-axis), at 30 min (left) and 2 h (right). In all plots (B-C, E-F, H-J), data are shown for control (blue) and cLTD (green) synapses (see Figure 6G for synapse counts). Asterisks indicate significant condition and condition-by-ASI perimeter interaction (int) effects for synapse subsets defined by d_{ag} (BH-adjusted *$p < 0.05$; see Table S1 for statistical details). Cluster legend in B applies to B-C, E-F, I-J.

Figure 9. Postsynaptic ultrastructure and astroglial coverage of synapses in the MML are mostly comparable to synapses in the OML under control conditions. (A) Stacked bar graphs showing the relative percentage of ASI^{ag-} (-, white, d_{ag} > 120 nm) versus ASI^{ag+} (+, sky blue, $d_{ag} \leq 120$ nm) synapses and **(B)** c1 (open) versus c2 (filled) synapses in each layer. Numbers above bars represent total synapse counts. **(C)** Kernel density estimate plots (KDE) showing the probability density function (PDF) for ASI perimeter (square-root axis) and **(D)** PSD area (log-scale axis). **(E)** Regression plots of the length of the ASI perimeter surrounded by astroglia within 120 nm (l_{ag}, square-root y-axis) and **(F)** the average astroglia distance to the ASI perimeter (avg d_{ag}, log-scale y-axis) versus ASI perimeter (square-root x-axis) for c1 or c2 synapses. Raw data and R^2 values are displayed. **(G)** KDE showing the PDF for PSD offset from the ASI center (log-scale axis) and **(H)** average distance between the ASI perimeter segment with astroglial apposition within 120 nm to the nearest PSD edge ($d_{agASI\text{-}PSD}$, log scale axis). In A-H, data are from control MML (dark blue) and OML (light blue) synapses (time points pooled), with only synapses with $d_{ag} \leq 120$ nm included in analyses plotted in B-H (see Figures 3G and 6G for synapse counts). Asterisks indicate significant layer and layer-by-ASI perimeter interaction (int) effects (*$p < 0.05$, **$p < 0.01$; see Table S1 for statistical details). Cluster legend in E applies to E-F.

Figure 10. Comparison of relative changes in tripartite synapse ultrastructure associated with LTP and cLTD in the dentate gyrus. (A) Kernel density estimate (KDE) plots showing the probability density function (PDF) for ASI perimeter (square-root axis) and **(B)** PSD area (log-scale axis). **(C)** Bar graphs show the percentage change in the length of the ASI perimeter surrounded by astroglia within 120 nm (l_{ag}) and **(D)** the average distance between astroglia and the ASI perimeter (d_{ag}) during LTP or cLTD relative to control. In C-D, percent changes were calculated after controlling for ASI perimeter, and separately for c1 (open bars) and c2 (filled bars) synapses. Stars above bars indicate significance levels for condition effects based on layer-specific analyses and error bars indicate standard errors. **(E)** KDE plots show the PDF for PSD offset (log-scale axis) and **(F)** the average distance between astroglia and the nearest PSD edge ($d_{agASI\text{-}PSD}$, log-scale axis). In A-F, data are from MML synapses during LTP (red) and OML synapses during cLTD (green) with $d_{ag} \leq 120$ nm, at 30 min (left) and 2 h (right) after LTP or cLTD induction (see Figures 3E, 3G, 6E, and 6G for synapse counts). *$p < 0.05$, ***$p < 0.001$ (see Table S1 for statistical details).

Figure 11. Summary of main effects on spines and PSDs. Under all conditions and spine sizes, the PSD was offset from the center of the ASI perimeter. The distribution of spine volumes and PSD areas expanded, increasing the frequency of both smaller and larger synapses at both 30 min and 2 h after the induction of LTP (red arrows). The ASI perimeter and PSD offset distributions shifted unidirectionally toward larger values at 2 h during LTP. In contrast, a shift towards spines with smaller ASI perimeters and less PSD offset from the ASI center and perimeter occurred transiently at 30 min during cLTD (green arrow).

Figure 12. Summary of main effects between perisynaptic astroglia and synapses. A) The length of astroglia (l_{ag}) apposed to the ASI perimeter was reduced by 30 min and further reduced by 2 h during LTP as spines and the ASI enlarged. The distances to the astroglia (d_{ag} and $d_{agASI\text{-}PSD}$) increased, resulting in reduced astroglial access to the PSD. **B)** In contrast, the length of the ASI perimeter and distances to the astroglia (d_{ag} and $d_{agASI\text{-}PSD}$) were decreased somewhat at small synapses by 30 min during cLTD, providing a transient increase in astroglial access to the PSD. **C)** Summary of effects at 30 min and 2 hr for LTP (red) and cLTD (green).

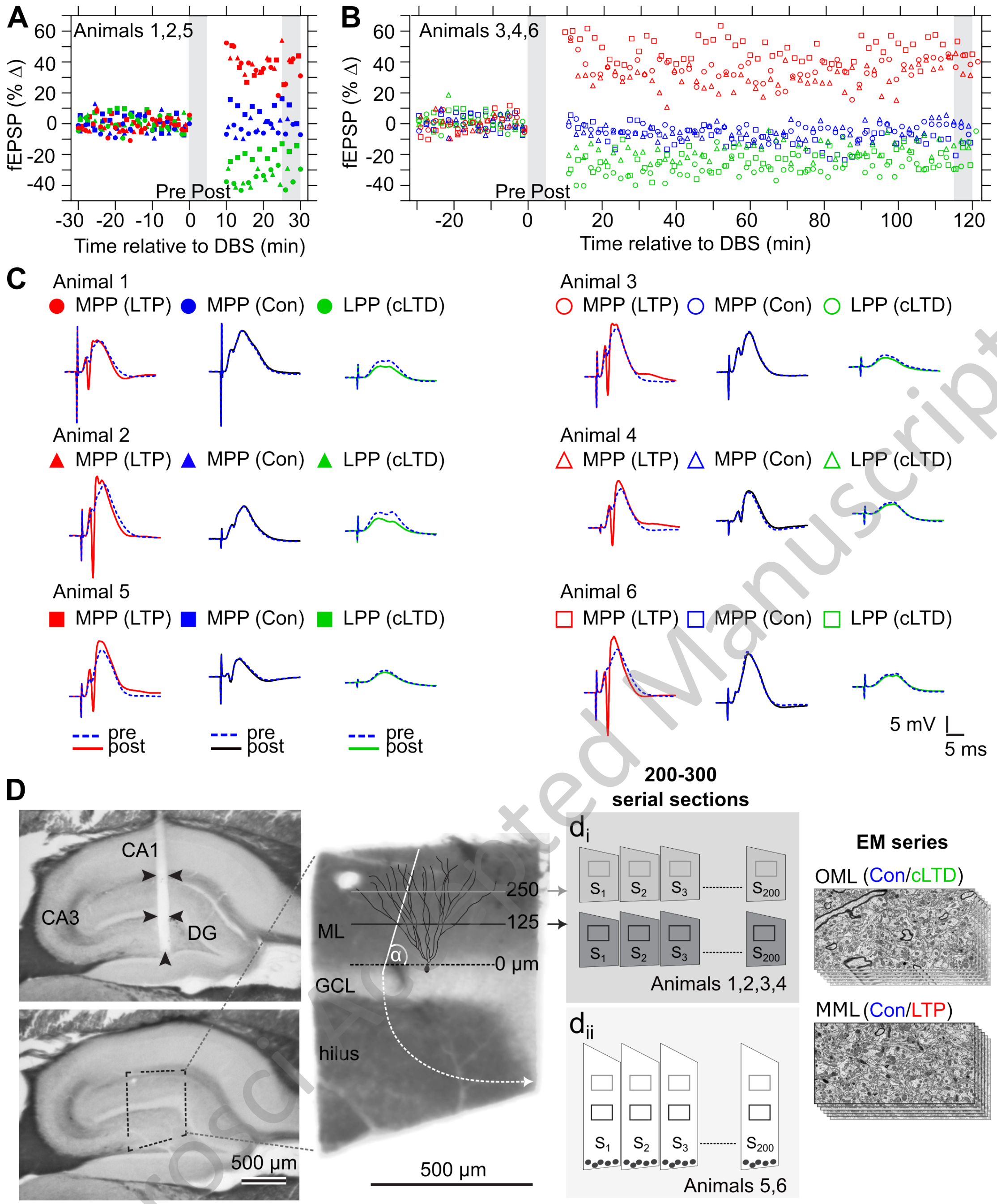
A
Animals 1,2,5
fEPSP (% Δ)
60
40
20
0
-20
-40
Pre
Post
-30
-20
-10
0
10
20
30
Time relative to DBS (min)
B
Animals 3,4,6
fEPSP (% Δ)
60
40
20
0
-20
-40
Pre
Post
-20
0
20
40
60
80
100
120
Time relative to DBS (min)
C
Animal 1
● MPP (LTP) ● MPP (Con) ● LPP (cLTD)
Animal 2
▲ MPP (LTP) ▲ MPP (Con) ▲ LPP (cLTD)
Animal 5
■ MPP (LTP) ■ MPP (Con) ■ LPP (cLTD)
Animal 3
○ MPP (LTP) ○ MPP (Con) ○ LPP (cLTD)
Animal 4
△ MPP (LTP) △ MPP (Con) △ LPP (cLTD)
Animal 6
□ MPP (LTP) □ MPP (Con) □ LPP (cLTD)
pre
post
pre
post
pre
post
5 mV
5 ms
D
CA1
CA3
DG
500 μm
ML
GCL
hilus
α
250
125
0 μm
500 μm
200-300
serial sections
d_i
S_1 S_2 S_3 S_{200}
S_1 S_2 S_3 S_{200}
Animals 1,2,3,4
d_{ii}
S_1 S_2 S_3 S_{200}
Animals 5,6
EM series
OML (Con/cLTD)
MML (Con/LTP)

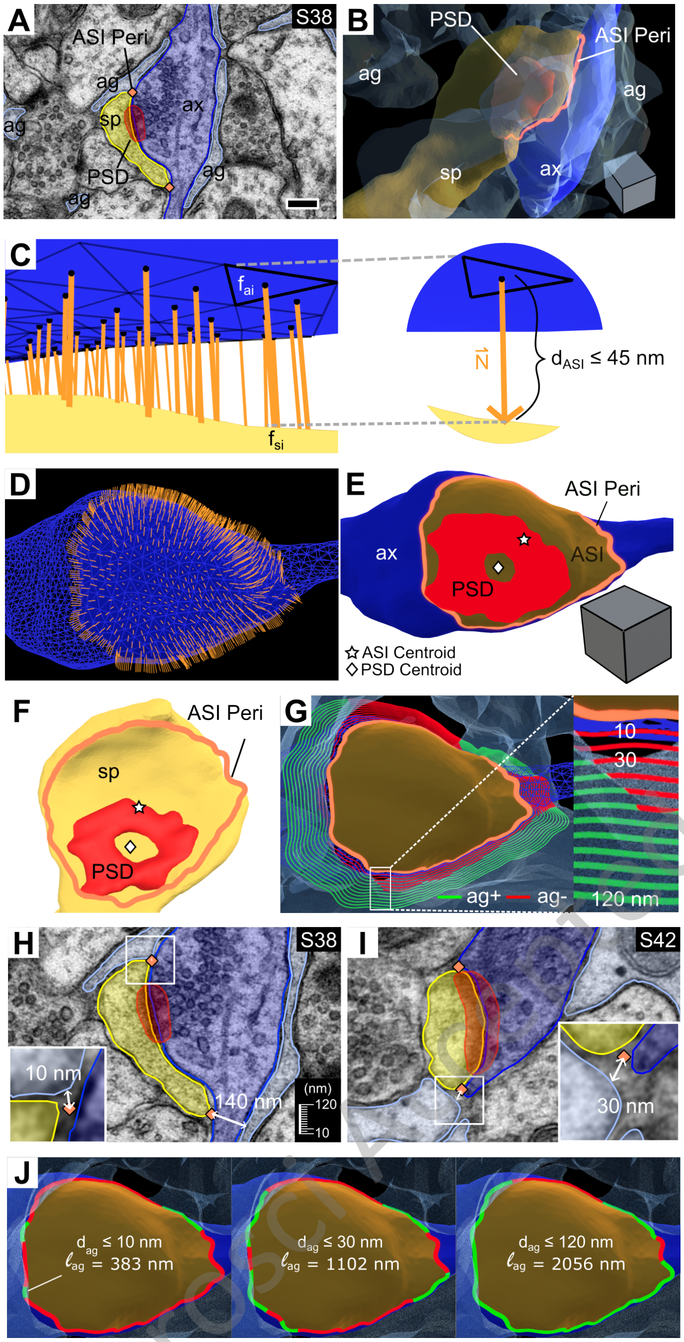
A
S38
ASI Peri
ag
ax
sp
ag
PSD
ag
ag
B
PSD
ASI Peri
ag
ag
sp
ax
C
f_{ai}
f_{si}
$\vec{N}$
$d_{ASI} \leq 45$ nm
D
E
ASI Peri
ax
ASI
PSD
☆ ASI Centroid
◇ PSD Centroid
F
ASI Peri
sp
PSD
G
10
30
ag+
ag-
120 nm
H
S38
10 nm
140 nm
(nm)
120
10
I
S42
30 nm
J
$d_{ag} \leq 10$ nm
$\ell_{ag} = 383$ nm
$d_{ag} \leq 30$ nm
$\ell_{ag} = 1102$ nm
$d_{ag} \leq 120$ nm
$\ell_{ag} = 2056$ nm

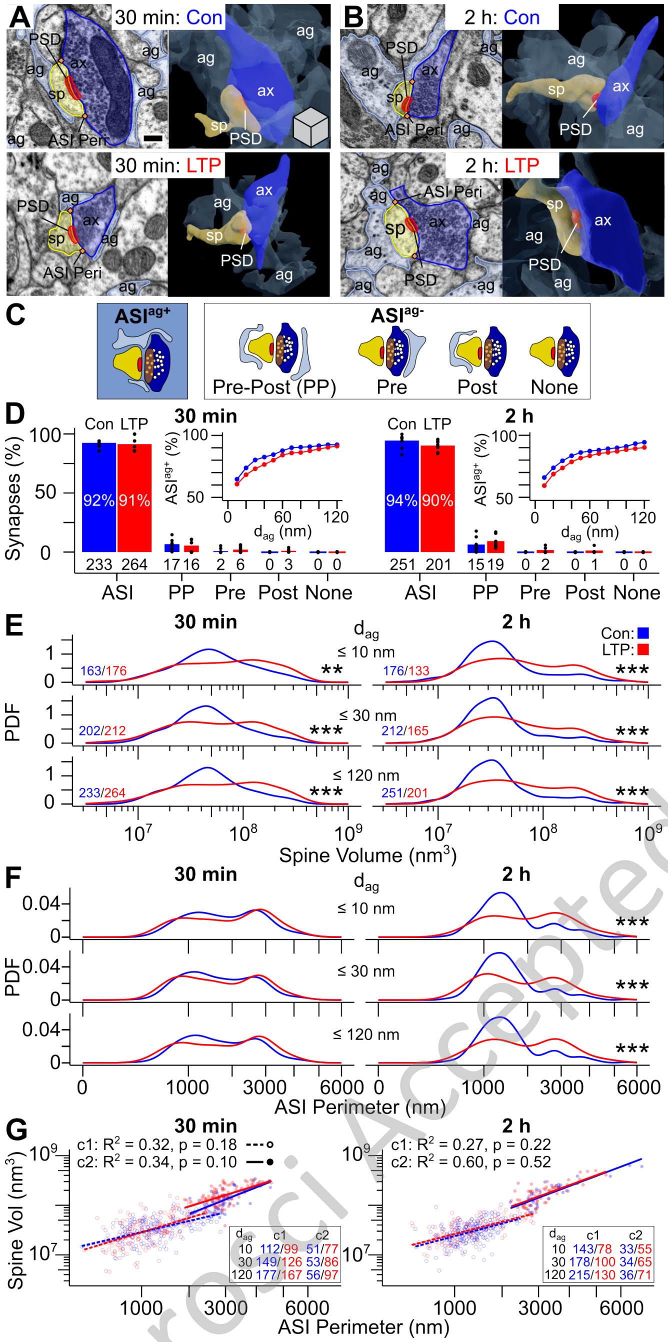
A
30 min: Con
30 min: LTP
B
2 h: Con
2 h: LTP
PSD
ag
ax
sp
ASI Peri
C
ASI^{ag+}
ASI^{ag-}
Pre-Post (PP)
Pre
Post
None
D
30 min
2 h
Con LTP
Synapses (%)
100
50
0
92%
91%
94%
90%
233 264 17 16 2 6 0 3 0 0
251 201 15 19 0 2 0 1 0 0
ASI PP Pre Post None
ASI^{ag+} (%)
d_{ag} (nm)
0 60 120
E
PDF
d_{ag}
≤ 10 nm
≤ 30 nm
≤ 120 nm
Con:
LTP:
163/176
176/133
202/212
212/165
233/264
251/201
**
***
10^7 10^8 10^9
Spine Volume (nm^3)
F
0.04
0
ASI Perimeter (nm)
0 1000 3000 6000
G
c1: R^2 = 0.32, p = 0.18
c2: R^2 = 0.34, p = 0.10
c1: R^2 = 0.27, p = 0.22
c2: R^2 = 0.60, p = 0.52
Spine Vol (nm^3)
10^9
10^7
d_{ag} c1 c2
10 112/99 51/77
30 149/126 53/86
120 177/167 56/97
d_{ag} c1 c2
10 143/78 33/55
30 178/100 34/65
120 215/130 36/71
1000 3000 6000

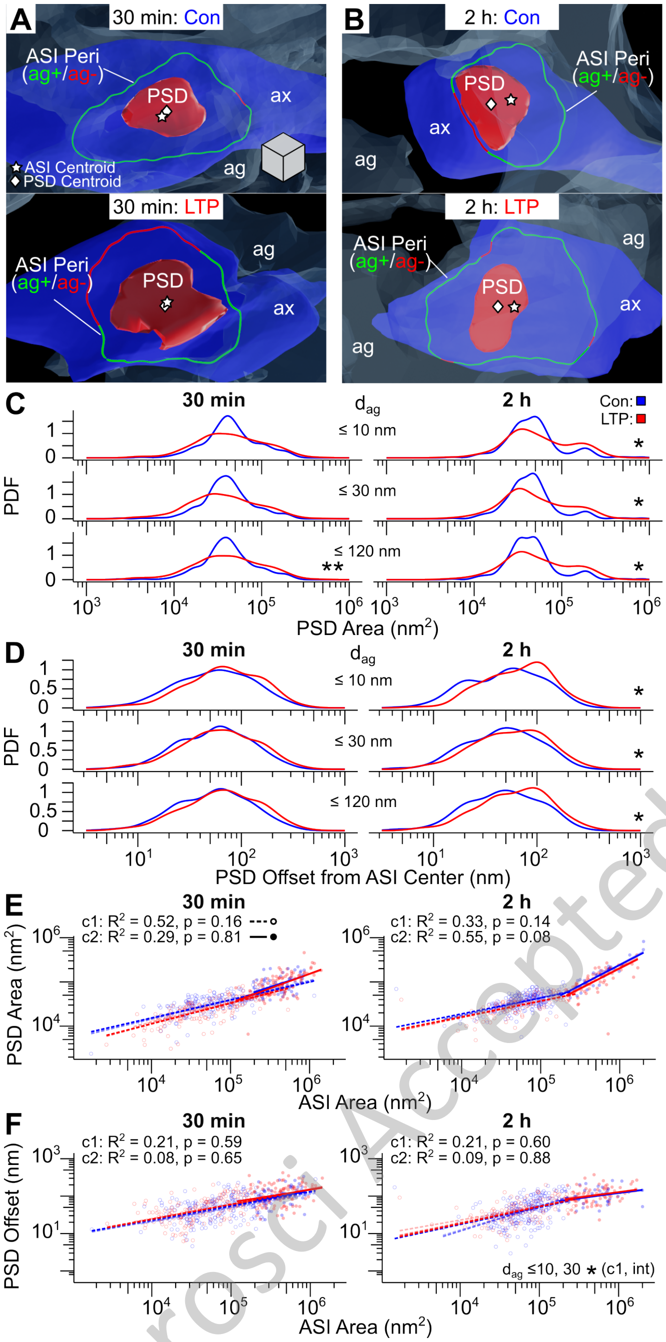
A
30 min: Con
ASI Peri
(ag+/ag-)
PSD
ax
ag
ASI Centroid
PSD Centroid
30 min: LTP
B
2 h: Con
2 h: LTP
C
30 min
2 h
d_{ag}
≤ 10 nm
≤ 30 nm
≤ 120 nm
Con:
LTP:
PDF
PSD Area (nm^2)
D
PSD Offset from ASI Center (nm)
E
c1: R^2 = 0.52, p = 0.16
c2: R^2 = 0.29, p = 0.81
c1: R^2 = 0.33, p = 0.14
c2: R^2 = 0.55, p = 0.08
PSD Area (nm^2)
ASI Area (nm^2)
F
c1: R^2 = 0.21, p = 0.59
c2: R^2 = 0.08, p = 0.65
c1: R^2 = 0.21, p = 0.60
c2: R^2 = 0.09, p = 0.88
PSD Offset (nm)
d_{ag} ≤10, 30 * (c1, int)
ASI Area (nm^2)

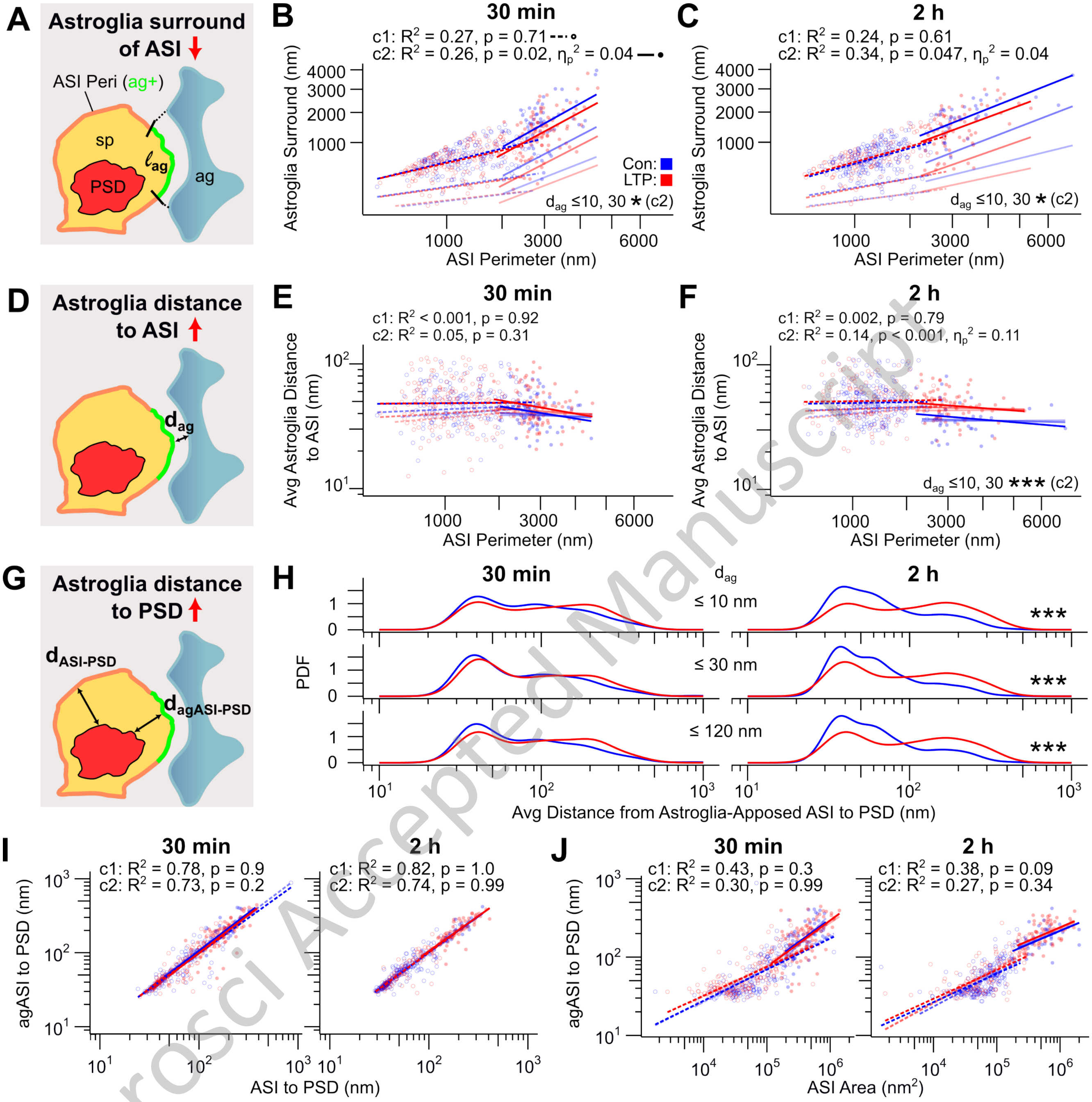
A
Astroglia surround of ASI
ASI Peri (ag+)
sp
PSD
ℓ_{ag}
ag
B
30 min
c1: R^2 = 0.27, p = 0.71
c2: R^2 = 0.26, p = 0.02, η_p^2 = 0.04
Astroglia Surround (nm)
4000
3000
2000
1000
Con:
LTP:
d_{ag} ≤10, 30 * (c2)
1000
3000
6000
ASI Perimeter (nm)
C
2 h
c1: R^2 = 0.24, p = 0.61
c2: R^2 = 0.34, p = 0.047, η_p^2 = 0.04
Astroglia Surround (nm)
4000
3000
2000
1000
d_{ag} ≤10, 30 * (c2)
1000
3000
6000
ASI Perimeter (nm)
D
Astroglia distance to ASI
d_{ag}
E
30 min
c1: R^2 < 0.001, p = 0.92
c2: R^2 = 0.05, p = 0.31
Avg Astroglia Distance to ASI (nm)
10^2
10^1
1000
3000
6000
ASI Perimeter (nm)
F
2 h
c1: R^2 = 0.002, p = 0.79
c2: R^2 = 0.14, p < 0.001, η_p^2 = 0.11
Avg Astroglia Distance to ASI (nm)
10^2
10^1
d_{ag} ≤10, 30 *** (c2)
1000
3000
6000
ASI Perimeter (nm)
G
Astroglia distance to PSD
$d_{ASI\text{-}PSD}$
$d_{agASI\text{-}PSD}$
H
30 min
d_{ag}
≤ 10 nm
2 h
***
≤ 30 nm
***
≤ 120 nm
***
PDF
1
0
10^1
10^2
10^3
Avg Distance from Astroglia-Apposed ASI to PSD (nm)
I
30 min
c1: R^2 = 0.78, p = 0.9
c2: R^2 = 0.73, p = 0.2
2 h
c1: R^2 = 0.82, p = 1.0
c2: R^2 = 0.74, p = 0.99
agASI to PSD (nm)
10^3
10^2
10^1
ASI to PSD (nm)
J
30 min
c1: R^2 = 0.43, p = 0.3
c2: R^2 = 0.30, p = 0.99
2 h
c1: R^2 = 0.38, p = 0.09
c2: R^2 = 0.27, p = 0.34
agASI to PSD (nm)
10^3
10^2
10^1
10^4
10^5
10^6
ASI Area (nm^2)

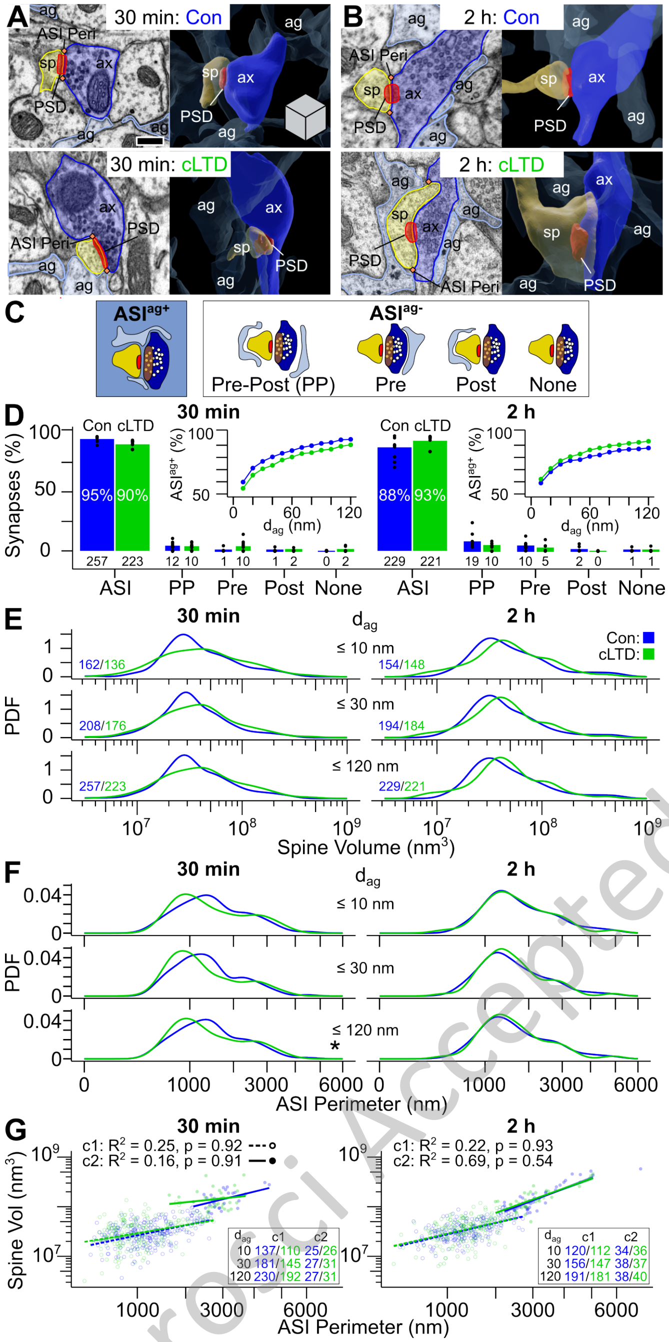
A
30 min: Con
30 min: cLTD
B
2 h: Con
2 h: cLTD
ag
ASI Peri
sp
ax
PSD
C
ASI^ag+
ASI^ag-
Pre-Post (PP)
Pre
Post
None
D
30 min
2 h
Con cLTD
Synapses (%)
100
50
0
95%
90%
88%
93%
257 223 12 10 1 10 1 2 0 2
229 221 19 10 10 5 2 0 1 1
ASI
PP
Pre
Post
None
ASI^ag+ (%)
d_ag (nm)
0
60
120
E
30 min
2 h
d_ag
≤ 10 nm
≤ 30 nm
≤ 120 nm
Con:
cLTD:
PDF
162/136
208/176
257/223
154/148
194/184
229/221
10^7
10^8
10^9
Spine Volume (nm^3)
F
30 min
2 h
d_ag
≤ 10 nm
≤ 30 nm
≤ 120 nm
*
PDF
0.04
0
0
1000
3000
6000
ASI Perimeter (nm)
G
30 min
c1: R^2 = 0.25, p = 0.92
c2: R^2 = 0.16, p = 0.91
2 h
c1: R^2 = 0.22, p = 0.93
c2: R^2 = 0.69, p = 0.54
Spine Vol (nm^3)
10^9
10^7
d_ag c1 c2
10 137/110 25/26
30 181/145 27/31
120 230/192 27/31
d_ag c1 c2
10 120/112 34/36
30 156/147 38/37
120 191/181 38/40
1000
3000
6000
ASI Perimeter (nm)

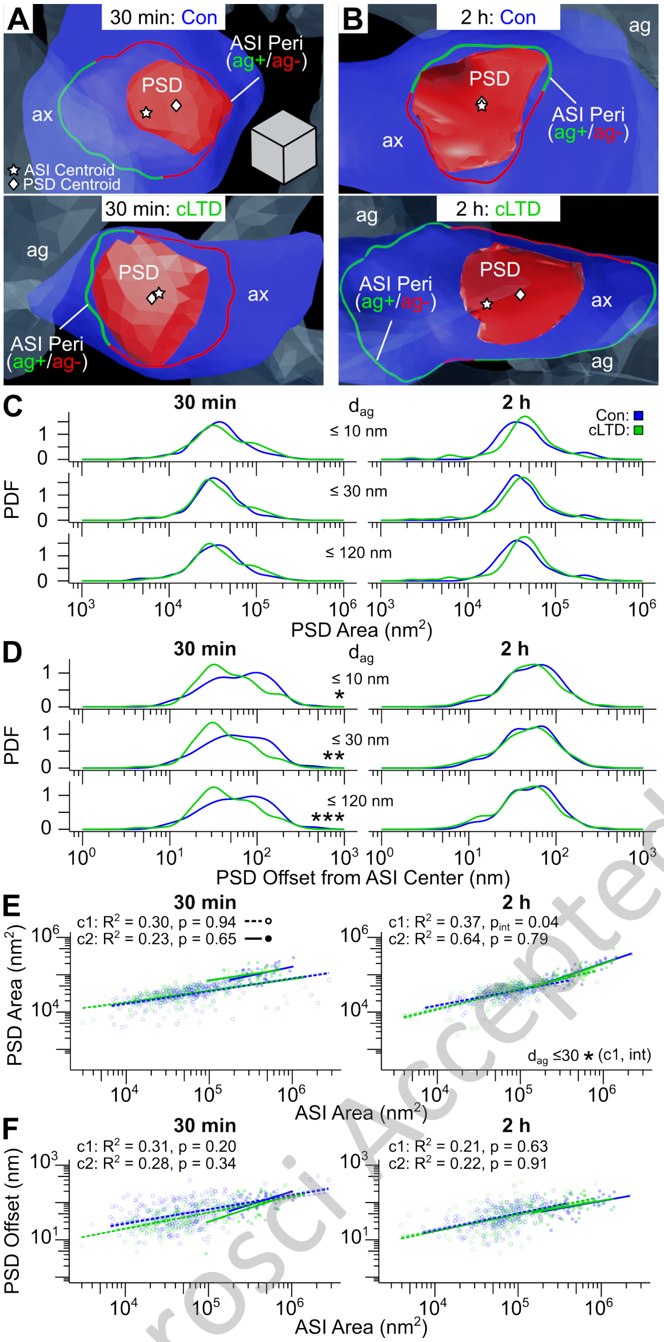
A
30 min: Con
ASI Peri
(ag+/ag-)
PSD
ax
ASI Centroid
PSD Centroid
B
2 h: Con
ag
PSD
ASI Peri
(ag+/ag-)
ax
30 min: cLTD
ag
PSD
ax
ASI Peri
(ag+/ag-)
2 h: cLTD
ag
ASI Peri
(ag+/ag-)
PSD
ax
ag
C
30 min
2 h
d_{ag}
Con: 🟦
cLTD: 🟩
≤ 10 nm
≤ 30 nm
≤ 120 nm
PDF
1
0
10^3
10^4
10^5
10^6
PSD Area (nm^2)
D
30 min
2 h
d_{ag}
≤ 10 nm
*
≤ 30 nm
**
≤ 120 nm
***
PDF
1
0
10^0
10^1
10^2
10^3
PSD Offset from ASI Center (nm)
E
30 min
c1: R^2 = 0.30, p = 0.94 ---○
c2: R^2 = 0.23, p = 0.65 —●
2 h
c1: R^2 = 0.37, p_{int} = 0.04
c2: R^2 = 0.64, p = 0.79
PSD Area (nm^2)
10^6
10^4
d_{ag} ≤30 ★ (c1, int)
10^4
10^5
10^6
ASI Area (nm^2)
F
30 min
c1: R^2 = 0.31, p = 0.20
c2: R^2 = 0.28, p = 0.34
2 h
c1: R^2 = 0.21, p = 0.63
c2: R^2 = 0.22, p = 0.91
PSD Offset (nm)
10^3
10^1
10^4
10^5
10^6
ASI Area (nm^2)

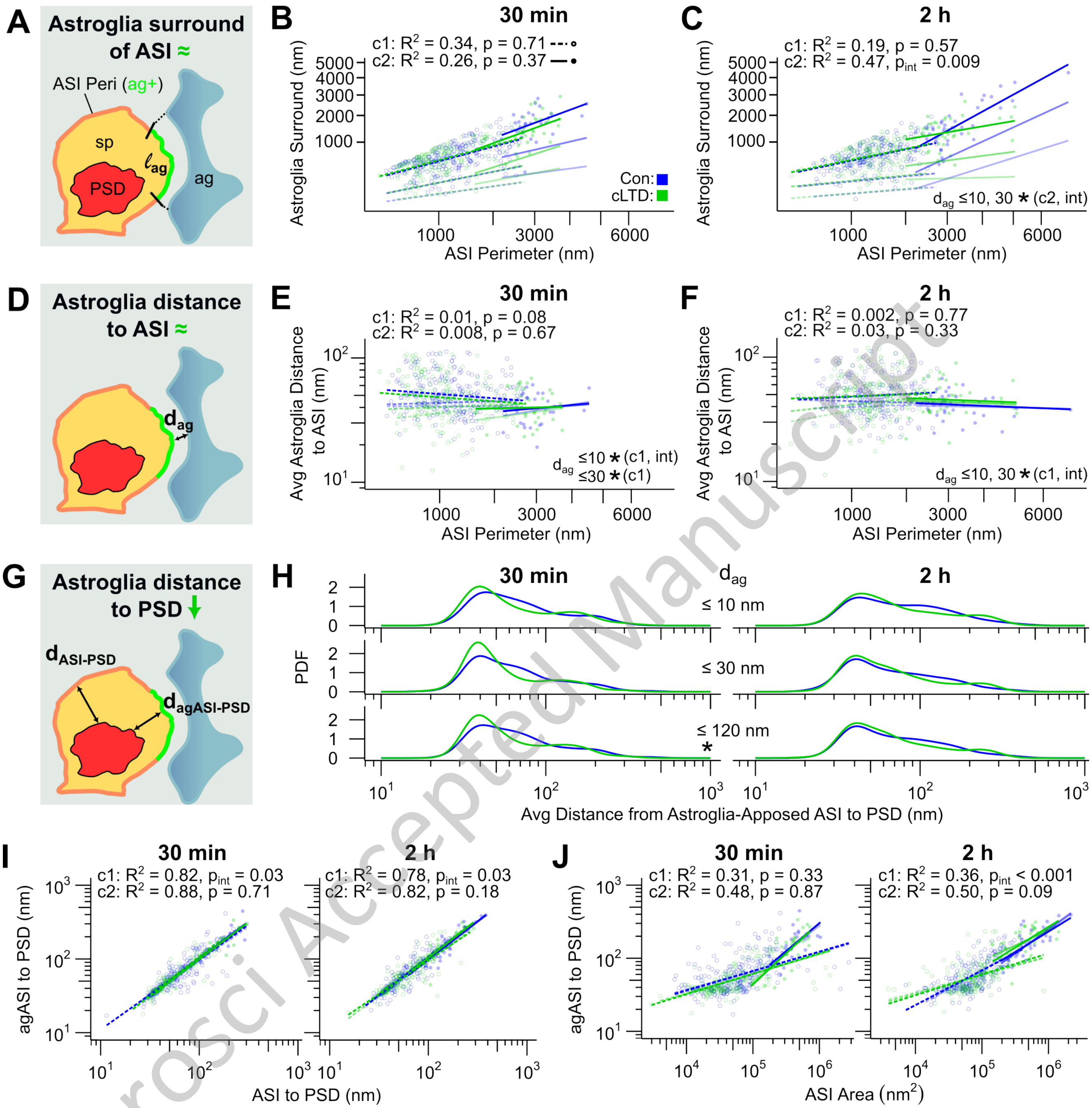
A
Astroglia surround of ASI ≈
ASI Peri (ag+)
sp
PSD
ℓ_{ag}
ag
B
30 min
c1: R^2 = 0.34, p = 0.71
c2: R^2 = 0.26, p = 0.37
Astroglia Surround (nm)
5000
4000
3000
2000
1000
Con: 🟦
cLTD: 🟩
1000
3000
6000
ASI Perimeter (nm)
C
2 h
c1: R^2 = 0.19, p = 0.57
c2: R^2 = 0.47, p_{int} = 0.009
Astroglia Surround (nm)
d_{ag} ≤10, 30 * (c2, int)
ASI Perimeter (nm)
D
Astroglia distance to ASI ≈
d_{ag}
E
30 min
c1: R^2 = 0.01, p = 0.08
c2: R^2 = 0.008, p = 0.67
Avg Astroglia Distance to ASI (nm)
10^2
10^1
d_{ag} ≤10 * (c1, int)
≤30 * (c1)
ASI Perimeter (nm)
F
2 h
c1: R^2 = 0.002, p = 0.77
c2: R^2 = 0.03, p = 0.33
Avg Astroglia Distance to ASI (nm)
d_{ag} ≤10, 30 * (c1, int)
ASI Perimeter (nm)
G
Astroglia distance to PSD ↓
$d_{ASI-PSD}$
$d_{agASI-PSD}$
H
30 min
2 h
d_{ag}
≤ 10 nm
≤ 30 nm
≤ 120 nm
*
PDF
2
1
0
10^1
10^2
10^3
Avg Distance from Astroglia-Apposed ASI to PSD (nm)
I
30 min
c1: R^2 = 0.82, p_{int} = 0.03
c2: R^2 = 0.88, p = 0.71
2 h
c1: R^2 = 0.78, p_{int} = 0.03
c2: R^2 = 0.82, p = 0.18
agASI to PSD (nm)
ASI to PSD (nm)
J
30 min
c1: R^2 = 0.31, p = 0.33
c2: R^2 = 0.48, p = 0.87
2 h
c1: R^2 = 0.36, p_{int} < 0.001
c2: R^2 = 0.50, p = 0.09
agASI to PSD (nm)
10^4
10^5
10^6
ASI Area (nm^2)

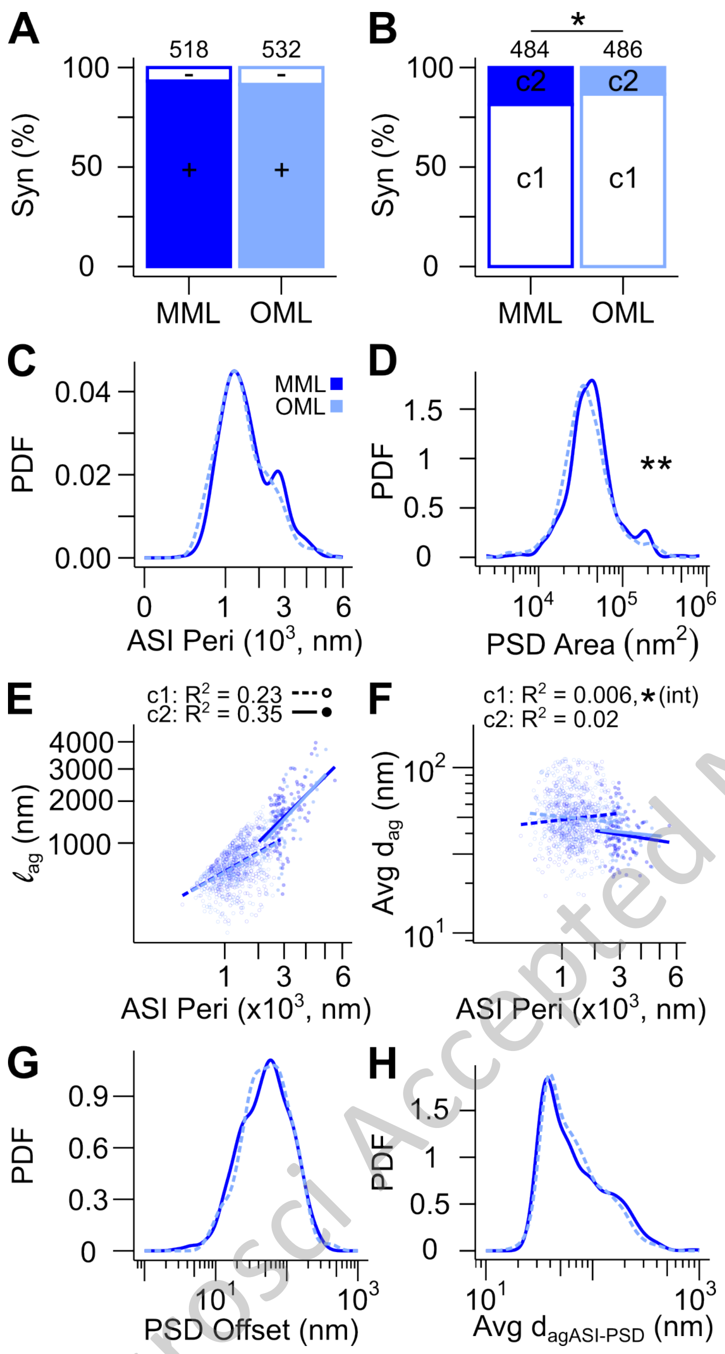
A
518
532
100
50
0
Syn (%)
-
+
MML
OML
B
*
484
486
c2
c1
C
0.04
0.02
0.00
PDF
MML
OML
0
1
3
6
ASI Peri (10^3, nm)
D
1.5
1
0.5
**
10^4
10^5
10^6
PSD Area (nm^2)
E
c1: R^2 = 0.23
c2: R^2 = 0.35
4000
3000
2000
1000
ℓag (nm)
ASI Peri (x10^3, nm)
F
c1: R^2 = 0.006, *(int)
c2: R^2 = 0.02
10^2
10^1
Avg dag (nm)
G
0.9
0.6
0.3
10^1
10^3
PSD Offset (nm)
H
Avg dagASI-PSD (nm)

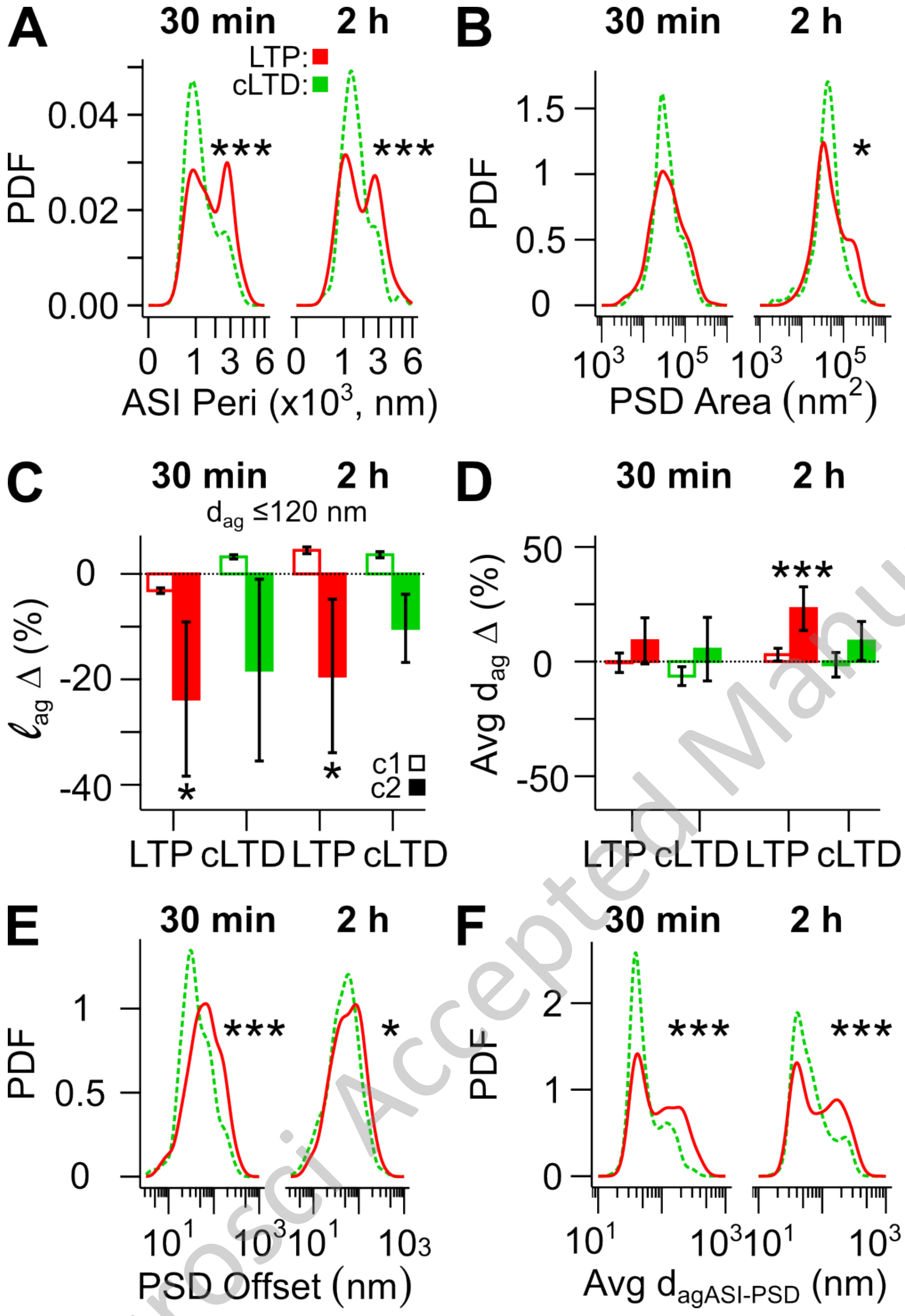
A
30 min
2 h
LTP: 🟥
cLTD: 🟩
PDF
0.04
0.02
0.00
***
***
0
1
3
6
ASI Peri (x10^3, nm)
B
30 min
2 h
PDF
1.5
1
0.5
0
*
10^3
10^5
PSD Area (nm^2)
C
30 min
2 h
d_{ag} ≤120 nm
ℓ_{ag} Δ (%)
0
-20
-40
*
*
c1 ☐
c2 ■
LTP
cLTD
LTP
cLTD
D
30 min
2 h
Avg d_{ag} Δ (%)
50
0
-50
***
LTP
cLTD
LTP
cLTD
E
30 min
2 h
PDF
1
0.5
0
***
*
10^1
10^3
PSD Offset (nm)
F
30 min
2 h
PDF
2
1
0
***
***
10^1
10^3
Avg $d_{agASI\text{-}PSD}$ (nm)

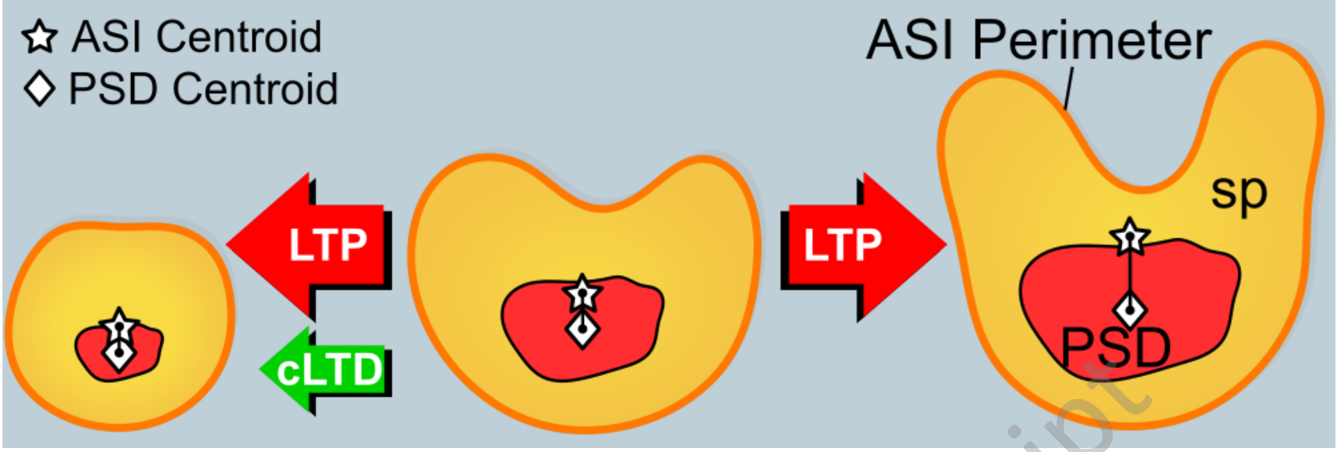
☆ ASI Centroid
◇ PSD Centroid
ASI Perimeter
LTP
cLTD
LTP
sp
PSD

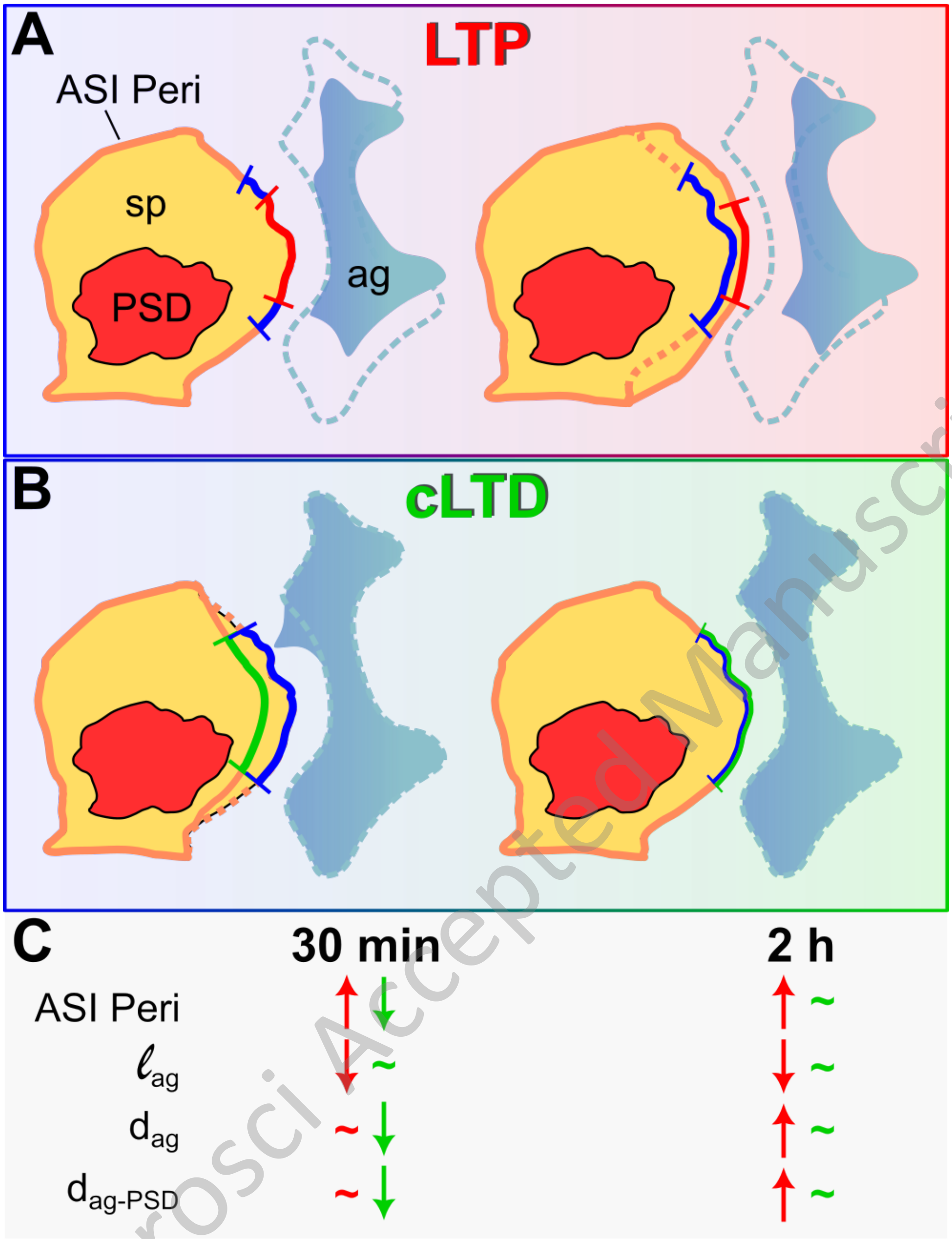
A
LTP
ASI Peri
sp
PSD
ag
B
cLTD
C
30 min
2 h
ASI Peri ↑ ↓ ↑ ~
ℓag ↓ ~ ↓ ~
dag ~ ↓ ↑ ~
dag-PSD ~ ↓ ↑ ~